

Contents

1	1	Gas Electron Multiplier	3
2	1.1	Introduction	3
3	1.2	Design and working principle of GEM detector	5
4	1.3	GEM for the CMS Phase-II Upgrade	7
5	1.3.1	CMS GE1/1 Detector Specification	10
6	1.3.2	GE1/1 Beam Test Studies	12
7	1.3.3	Beam Test Experimental Set-up	16
8	1.3.4	Data Analysis	17
9	1.4	Characterization and Production of GEM Foil	32
10	1.4.1	Visual Inspection	34
11	1.4.2	Optical Test	34
12	1.4.3	Electrical Test	36
13	Appendices		41
14	A	GE11 detector generations	43
15	B	Gaseous Detector Important Points	45
16	B.1	Gain Measurement	45
17	B.2	Transparancy	46

19	B.3 Charge-up effect	46
20	B.4 Townsend coefficient	47
21	B.5 Raether Limit	47
22	B.6 Collection efficiency	48
23	C GE1/1 measured parameters	49
24	D Efficiency and Time Resolution Fit Parameters	53
25	D.1 Efficiency Vs E_{gain}	53
26	D.1.1 Fit Parameters	53
27	D.2 Efficiency Vs current	56
28	D.2.1 Fit Parameters	56
29	D.3 Efficiency Vs Drift Voltage	58
30	D.3.1 Fit Parameters	58

³¹ **1**

³² **Gas Electron Multiplier**

³³ “*New directions in science are launched by new tools much more often than
34 by new concepts.*”

³⁵ – Freeman Dyson

³⁶ In this chapter, the GEM detector technology is introduced which are proposed for
³⁷ the CMS muons system upgrade during the long shutdown-2 period. The properties
³⁸ of these GEM detectors were scrutinized during different beam test campaigns carried
³⁹ out at the CERN SPS beam test facility. The first half of this chapter deals with
⁴⁰ the measurements performed on prototypes of CMS GEM detectors using the data
⁴¹ collected during different beam tests. The characterisation of GEM foils developed
⁴² in India for the CMS upgrade is described in the last part of the chapter.

⁴³ **1.1 Introduction**

⁴⁴ The invention of Multi-Wire Proportional Chamber (MWPC) in 1968 by Georges
⁴⁵ Charpak was one of the major breakthroughs in the development of gaseous detec-
⁴⁶ tors since it had better rate capability vis-a-vis its predecessors [1]. This invention

47 also led to a Nobel prize for George Charpak in 1992. The design and performance
48 of MWPC have improved progressively through all these years. However, because of
49 our increasing demands with the acquired knowledge about particle detection, it has
50 reached its limitation in terms of the maximum rate capability and detector granu-
51 larity. In 1988, Anton Oed invented the Micro-Strip Gas Counter (MSGC) which had
52 a position resolution of few tens of microns and could overcome the rate limitation
53 arising due to positive-ion accumulation in the gas volume. Also, it could sustain a
54 particle flux greater than few MHz/mm^2 . Although, these kinds of detectors were
55 very impressive the long-term study revealed the following shortcomings:

- 56 1. Accumulation of ions on the electrodes, which affects the gain and age of the
57 detector.
- 58 2. In some cases, the passage of highly ionising particles could lead to a destructive
59 discharge in the detector medium.

60 These drawbacks of the MSGC lead to the development of Micro-Pattern Gaseous
61 Detectors (MPGD). This class of detectors, specifically the Gas Electron Multiplier
62 (GEM) [2, 3, 4], could provide an unprecedented spatial resolution, larger sensi-
63 tive/detection area, with higher rate capability and good operational stability over
64 the longer operating periods. Several new studies also revealed that under certain cir-
65 cumstances these detectors might be less vulnerable to the radiation-induced ageing
66 than the standard silicon microstrip detectors [5, 6].

67 Because of their efficient detection qualities and high rate capabilities, GEM detec-
68 tors have already been used in various experiments like COMPASS, TOTEM, LHCb.
69 Recently, it was proposed for the CMS muon detector system upgrade. A brief de-
70 scription of the working and properties of GEM detectors is provided in the following
71 sections.

72 1.2 Design and working principle of GEM detector

73 GEM is a relatively new concept introduced by Fabio Sauli [2] at CERN, which
74 consists of a thin polyimide sheet (usually a thin Kapton foil [7] with thickness 50
75 μm) coated with metal on its both sides. It is chemically pierced to a regular array of
76 holes using the photolithography and acid etching processes [8], as shown in Fig. 1.1
(left).

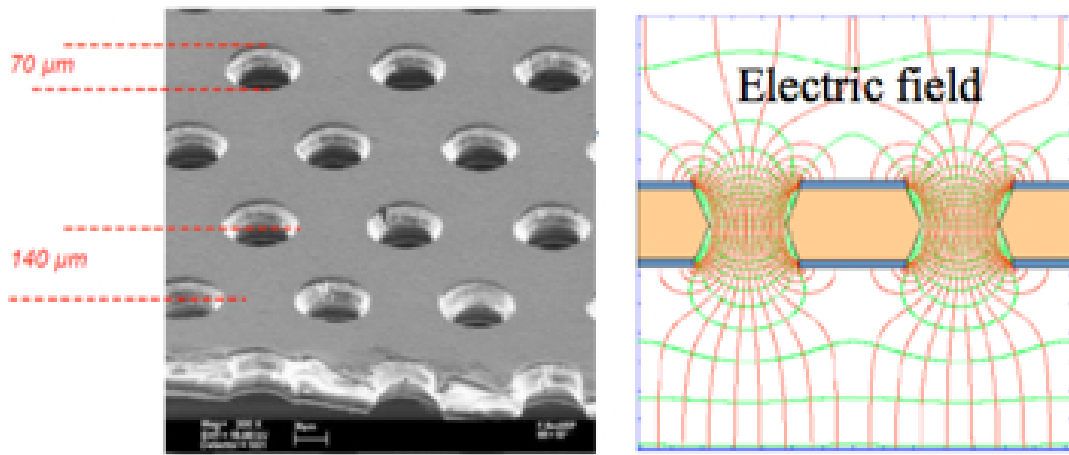


Figure 1.1: A cross-sectional view of a GEM foil etched with holes (left). The strong electric field generated in the vicinity and inside of the holes on the application of the potential across the foil (right).

77

A potential difference is applied between the two copper layers which create a high electric field inside the holes (Fig. 1.1) and is given as

$$E = \frac{V}{d} \quad (1.1)$$

78 where E is the electric field inside a hole in the GEM foil, V is the voltage applied
79 between the two copper layers and d is the thickness of the GEM foil.

80 To illustrate the working of a GEM detector, the active detector medium could
81 be divided into three different regions: drift, amplification and induction regions, as

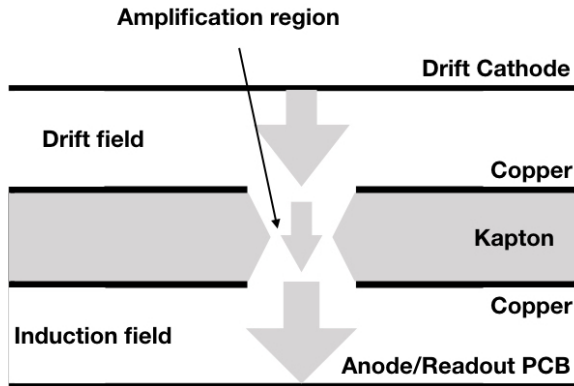


Figure 1.2: Outline of a single GEM detector.

82 shown in Fig. 1.2. The passage of a charged particle leads to ionization in the drift
 83 region, and the generated primary electrons drift towards the amplification region
 84 (i.e., through GEM holes). The electrons gain kinetic energy from the intense electric
 85 field inside the holes sufficient to produce secondary ionizations, eventually, leading
 86 to an avalanche multiplication. Finally, in the induction region, all the electrons from
 87 the amplification regions are collected on the readout plane.

88 To avoid the problem of electrical breakdown, several GEM foils operating at lower
 89 voltages, are stacked together in between the drift cathode and the readout board.
 90 For such detector configurations, the transfer region takes almost all the electrons
 91 from one GEM foil to another. In view of the fact that the total gain of a detector is
 92 given as the product of the individual gain of each foil, gains up to an order of 10^5 can
 93 be achieved in this way. In this configuration, the detector can reach its maximum
 94 gain without any or with the least probability of electric discharge.

95 The gain and discharge probability are compared for the single, double and triple-
 96 layered GEM detectors as shown in Fig. 1.3, which clearly indicates that the triple
 97 GEM detectors can achieve a gain beyond 10^4 without any electrical discharge. Also,
 98 the signal readout by the electrode is pretty fast as it uses only electrons to read the

99 signal. Multi-layered boards could be used to achieve a two-dimensional readout from
these detectors.

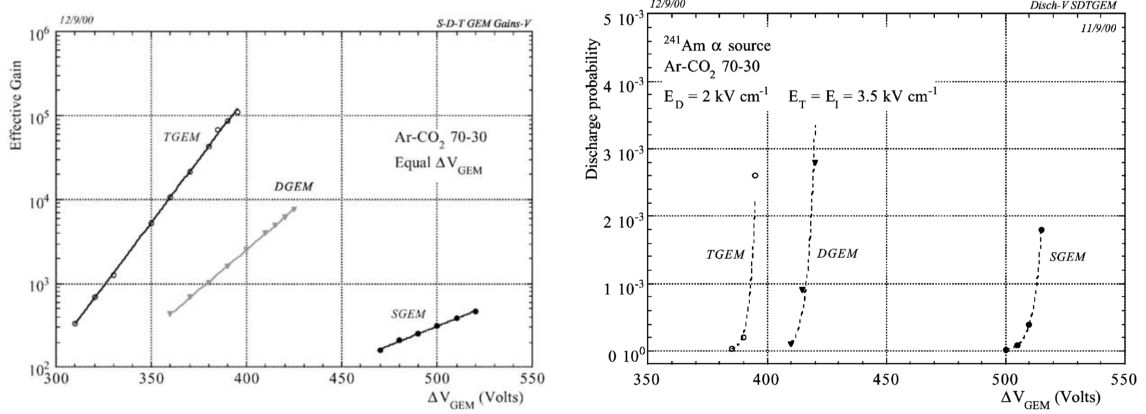


Figure 1.3: Comparison of total effective gain on anode as a function of applied voltage for single, double and triple layered GEM detectors (left). The discharge probability as a function of applied voltage is shown for the single, double and triple layered GEM detectors (right) [9].

100
101 A detector arrangement where three GEM foils are stacked together is known as
102 a “***Triple-GEM detector***”, as shown in Fig. 1.4. Such a detector configuration is
proposed for the CMS Phase-II upgrade and is discussed in the following section.

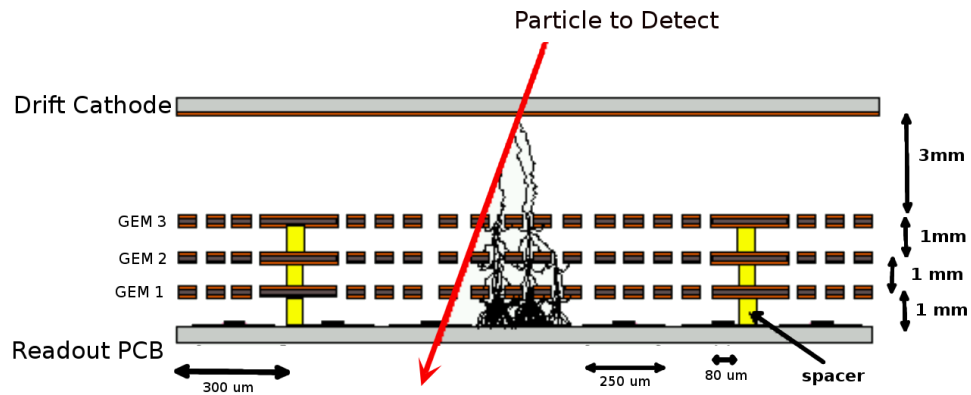


Figure 1.4: The working mechanism of a GEM detector.

104 1.3 GEM for the CMS Phase-II Upgrade

105 As pointed out in Sec. ??, the CMS Collaboration has finalised to install GEM detec-
106 tors in the pseudo-rapidity region $1.6 < |\eta| < 2.2$. These detectors will support the
107 existing CSC muon sub-system to improve the muon triggering and tracking capabil-
108 ities in the forward region [10]. The combined operation of CSC and GEM detectors
109 will lead to a precise measurement of the muon bending angle at the trigger level,
110 thus strongly reducing the rate of muon mis-reconstruction.

111 This CMS muon detector system upgrade is carried out to achieve the following
112 goals:

- 113 • Re-establish the redundancy in the forward region beyond $\eta = 1.6$
- 114 • Improve the muon tracking performance during the high-luminosity LHC oper-
115 ation.

116 The installation of GEM detectors is proposed during the period of Long Shutdown-
117 2 (2019-2020). The upgrade project is named as CMS GE1/1 upgrade, where the
118 letter “G” stands for GEM, “E” stands for End-cap, the first “1” corresponds to the
119 first muon station and the second “1” corresponds to the first ring of the station.
120 Analogously, the GEM detectors to be installed in the CMS detector are referred to
121 as GE1/1 detectors. The detectors will be inserted in front of the ME1/1 station and
122 into the slots originally foreseen for the RPC detectors, as shown in Fig. 1.5.

123 1.3.1 CMS GE1/1 Detector Specification

124 A typical GE1/1 detector is trapezoidal in shape with an active area of $990 \times (220 -$
125 $445) \text{ mm}^2$. The shape and size of the detector was decided based on the geometry of
126 vacant high- η region in the CMS muon endcap regions. A GE1/1 chamber consists of

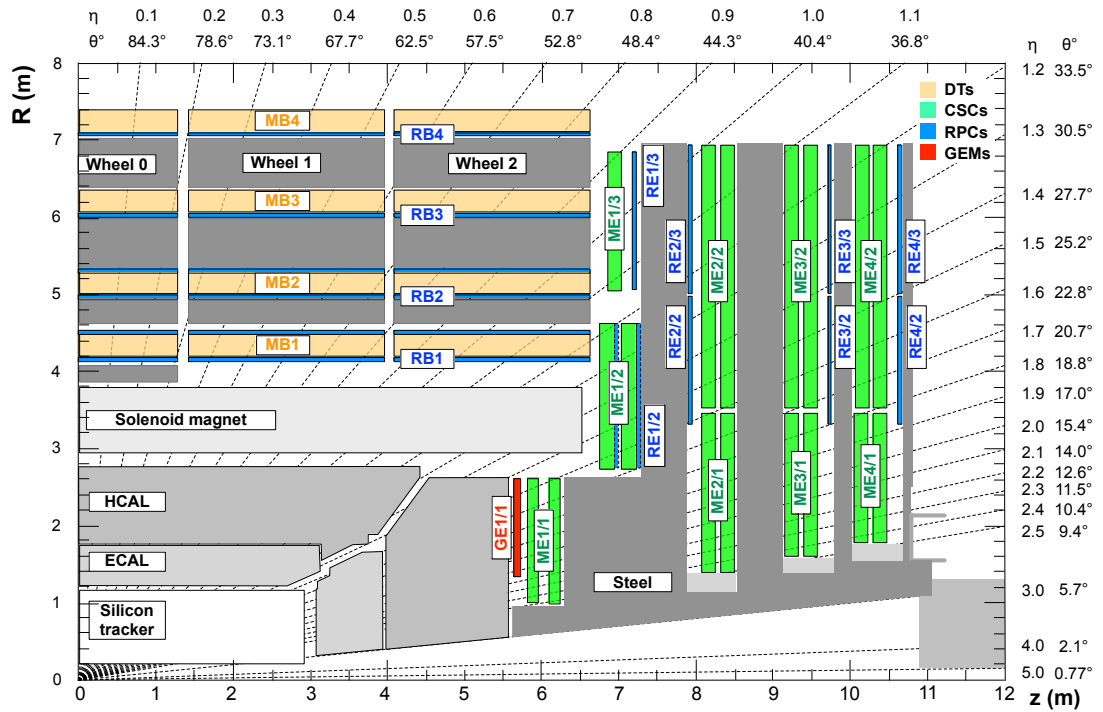


Figure 1.5: A cross-sectional view of the CMS quadrant highlighting the location of GEM detectors (red).

¹²⁷ a Triple-GEM detector having a 3/1/2/1 mm (drift/transfer 1/transfer 2/induction) electrode gap configuration, as shown in Fig. 1.6. The GEM foil consists of a thin

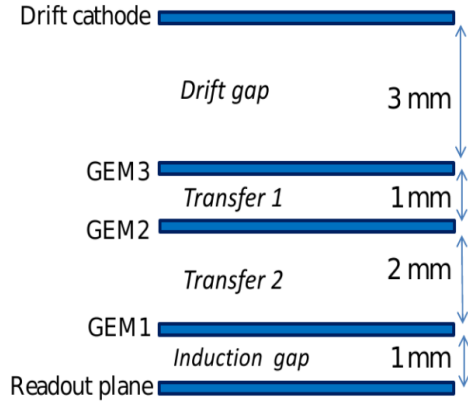


Figure 1.6: The layout of different GEM layers inside a CMS GE1/1 detector.

¹²⁸

¹²⁹ Kapton foil ($50 \mu m$ thick) with a copper clad ($5 \mu m$) on both sides. The detector
¹³⁰ readout board is divided into eight η -partitions with 384 strips. Each strip is radially
¹³¹ oriented along the long side of the detector with a pitch varying from $0.6 mm$ (short
¹³² side) to $1.2 mm$ (long side). Each partition is subdivided along the ϕ -coordinate
¹³³ into three readout sectors with 128 strips or channels per sector. The η partition
¹³⁴ and ϕ portions of the GEM detector are shown in Fig. 1.7. To improve tracking
¹³⁵ capabilities, two GEM chambers will be mounted face-to-face to form a double layer
¹³⁶ called “*Super-Chamber*”. Thus each Super-Chamber will provide two impact points
¹³⁷ for each muon track. The full layer by layer mechanical design of a GEM chamber
¹³⁸ is shown in Fig. 1.8. The main parts in a GEM detector are GEM foil, drift plane,
¹³⁹ readout board, shielding, high voltage divider, etc.

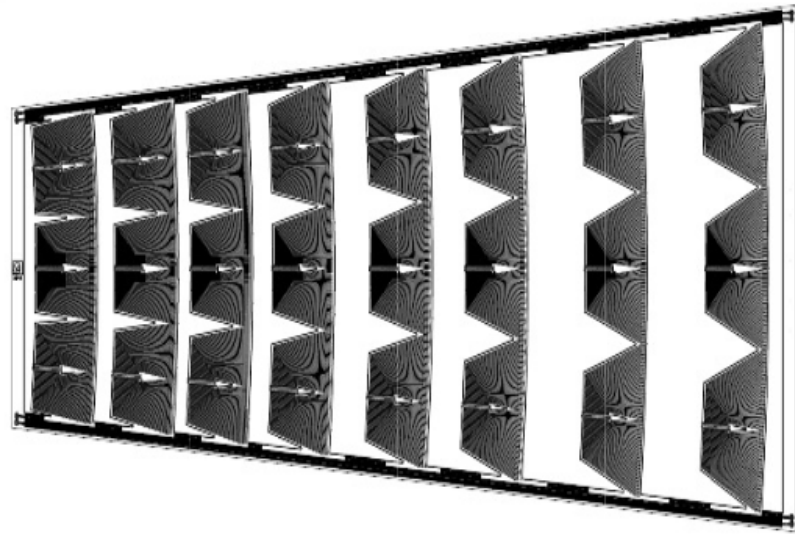


Figure 1.7: Drawing of a large trapezoidal CMS GEM chamber showing $8 - \eta$ and $3 - \phi$ par partitions.

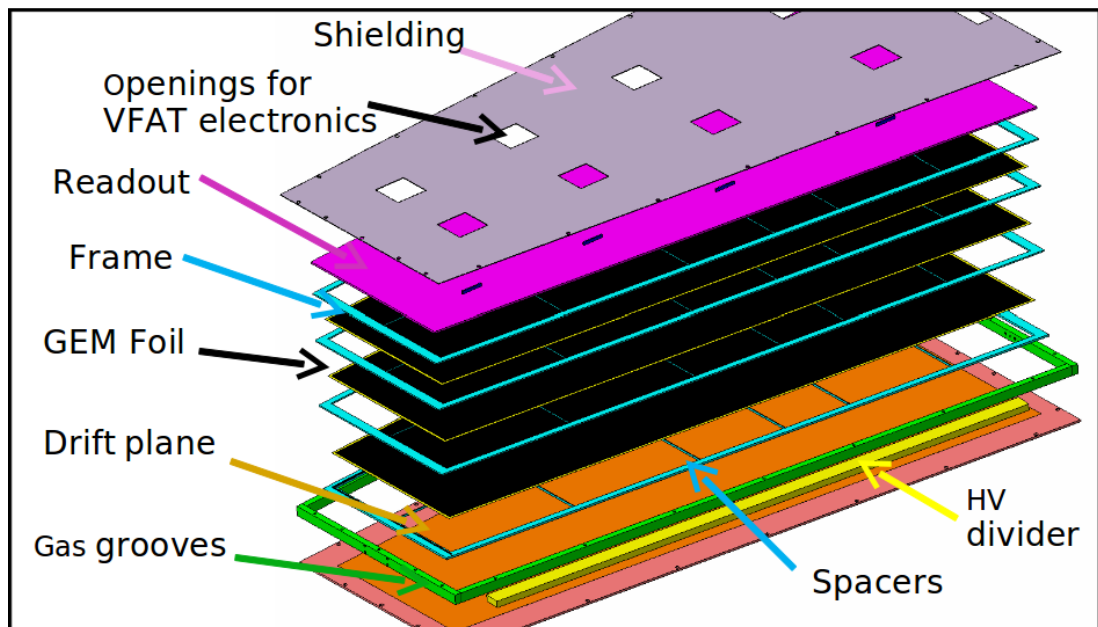


Figure 1.8: Layer by layer view of GEM detector

¹⁴⁰ **1.3.2 GE1/1 Beam Test Studies**

¹⁴¹ The GE1/1 detector was tested using 150 GeV muon and pion beams at CERN SPS
¹⁴² beam test facility during October-December 2014.

¹⁴³ The goal of the beam test campaign was to measure the efficiency, space & time
¹⁴⁴ resolution, and the cluster size of the CMS GEM detector. The detectors that
¹⁴⁵ were tested included GE11_IV and GE11_IV_GIF detectors. Both GE11_IV and
¹⁴⁶ GE1/1_IV_GIF are generation¹ IV GE1/1 detectors but GE1/1_IV_GIF was irra-
¹⁴⁷ diated with the gamma-ray at the CERN gamma-ray irradiation facility² for 1 year
¹⁴⁸ to perform ageing studies [11]. Also, several important parameters like electric field,
¹⁴⁹ voltage across each GEM foil and the rate and gain were measured and shown in
¹⁵⁰ appendix C.

¹⁵¹ Two beam test campaign was carried out during October-December 2014. These
¹⁵² campaigns were held in H2 and H4 beam test area of CERN SPS. The H2 beam test
¹⁵³ was held from 6th October 2014 to 27th October 2014 while the H4 beam test was
¹⁵⁴ held from 26 November to 14 December 2014. The main goal of the H2 beam test was
¹⁵⁵ to test the two detectors mentioned above with an Ar : CO₂ gas mixture while in H4
¹⁵⁶ beam test the same detector was tested with Ar : CO₂ : CF₄ gas mixture. Initially,
¹⁵⁷ the plan was to scan each sector of the GEM detectors but due to timing constraints
¹⁵⁸ we were just able to scan sector $(i\eta, i\phi) = \{(5, 2)\}$ and $(i\eta, i\phi) = \{(1, 2), (5, 2), (8, 2)\}$
¹⁵⁹ during H2 and H4 beam test respectively.

¹⁶⁰ The data collected during these beam test campaigns were grouped into different
¹⁶¹ run names, based on the electronic setup and gas mixtures used during the data tak-

¹The different generations of GE1/1 are described in appendix A

²The GIF bunker contains a ¹³⁷Cs source of 566 GBq. This emits gamma rays of 662 keV. The detector was placed 30 cm from the source where the particle rate was of the order of 100 kHz/cm². This allowed accumulating the charge in twelve months which would be equivalent to the 10-year operation of GEM detector in LHC environment [11].

Run Name	Details
2014H2C	Run range: 306-407 Threshold for each VFAT strip = 15 VFAT units ³ = 1.2fC Asynchronous mode with respect to the LHC clock sector scanned ($i\eta, i\phi$) = (5, 2) Gas mixture used: Ar : CO ₂ =(70:30)
2014H4A	Run range: 1592-1646 Threshold for each VFAT strip = 15 VFAT units = 1.2fC Asynchronous mode with respect to the LHC clock sector scanned ($i\eta, i\phi$) = (5, 2) Gas mixture used: Ar : CO ₂ : CF ₄ =(40:15:45)
2014H4C	Run range: 1868-1906 Threshold for each VFAT strip = 15 VFAT units = 1.2fC Asynchronous mode with respect to the LHC clock sector scanned ($i\eta, i\phi$) = (8, 2) Gas mixture used: Ar : CO ₂ : CF ₄ =(40:15:45)
2014H4D	Run range: 2065-2123 Threshold for each VFAT strip = 15 VFAT units = 1.2fC Asynchronous mode with respect to the LHC clock sector scanned ($i\eta, i\phi$) = (1, 2) Gas mixture used: Ar : CO ₂ : CF ₄ =(40:15:45)

Table 1.1: List of golden runs used to measure the GE1/1 properties.

¹⁶² ing. Out of these four sets of run ranges were marked as “*good*”, based on certain data
¹⁶³ quality checks, for further analysis. These run ranges along with their specification
¹⁶⁴ are listed in Table 1.1.

¹⁶⁵ Readout Electronics

¹⁶⁶ Front-end electronics used in the beam test was **VFAT2** chips [12, 13]. The upgraded
¹⁶⁷ version of the same chip, known as VFAT3, will be used with GE1/1 detectors for
¹⁶⁸ Level-1 muon triggering [14]. Its block diagram is shown in Fig. 1.9.

¹⁶⁹ VFAT is a front-end Application Specific Integrated Circuit (ASIC) chip. It was
¹⁷⁰ primarily designed for the readout of sensors in the TOTEM experiment at CERN.

³¹ 1 VFAT unit = 0.08 fC

171 VFAT chip is used for both triggering and tracking purpose. For triggering it uses
172 the programmable “*fast OR*” information based on a hit in the detector. It provides
173 a monostable output for the programmed number of channels in a single clock cycle.
174 This is called an “*S-Bit*”. While, for tracking it provides the spatial information
175 strip-wise for every triggered event.

176 VFAT2 has 128 analog input channels, very low noise pre-amplifier, shaper and
177 comparator attached to it. Signal discrimination is done based on the programmable
178 threshold setting and then stored within SRAM⁴ until the trigger information is
179 received. It can apply positive as well as negative threshold value to each channel
180 independently. This feature is named as “*TrimDAC*” and it has two programmable
181 voltages V_{T1} and V_{T2} and the threshold is defined as the difference between these two
182 programmable voltages, i.e., $V_{TH} = V_{T2} - V_{T1}$.

183 This VFAT chip also provides the facility to mask individual noisy channel.
184 To synchronize the output of the comparator the monostable block provides 1 clock
185 pulse for each threshold-crossing signal.

186 **Latency** defines the correct moment of time at which VFAT2 will read the signal.
187 Technically, for a given trigger, it is defined as the number of SRAM locations the
188 chip has to go back in order to read the digital output of the event corresponding to
189 that trigger. It is measured in clock periods.

190 TURBO Readout Board

191 TURBO is a standalone DAQ system for the VFAT front-end ASIC [15]. It was
192 developed for testing TOTEM hybrid equipped with VFAT chips, with following

⁴Static random-access memory (static RAM or SRAM) is a type of semiconductor memory that uses bistable latching circuitry (flip-flop) to store each bit. SRAM exhibits data remembrance but it is still volatile in the conventional sense that data is eventually lost when the memory is not powered.

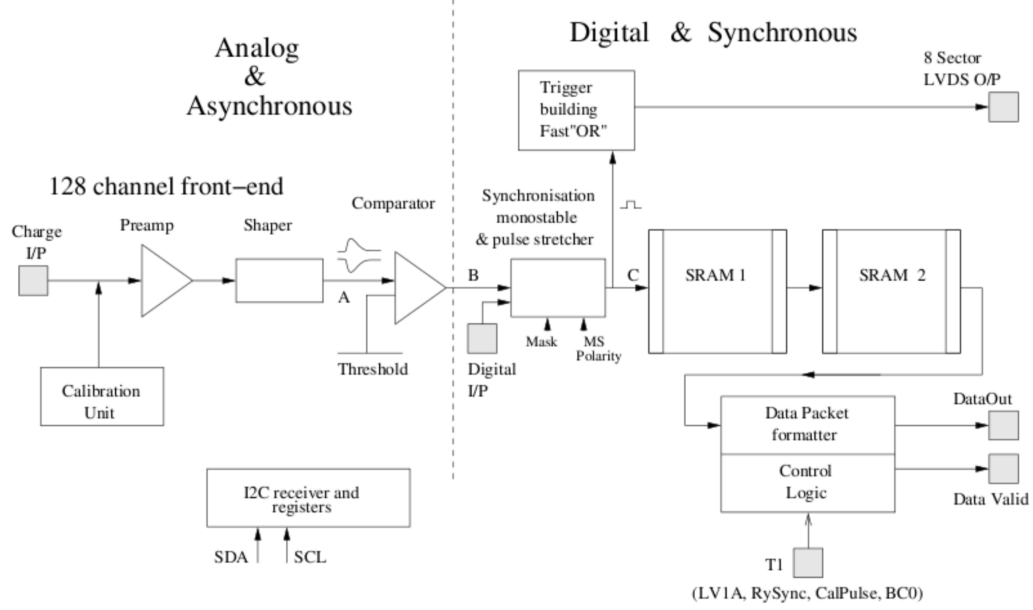


Figure 1.9: Block diagram of the VFAT2 chip showing signal flow [12].

193 goals:

- 194 • portable,
- 195 • real-time response,
- 196 • DAQ capability for small and medium-sized experiments.

197 Each TURBO can accommodate up to 8 VFAT chips. A systematic diagram of
 198 TURBO board is shown in Fig. 1.10. But, one can use more than 1 TURBO boards
 199 to accommodate more than 8 VFAT chips. Out of them, one TURBO board will act
 200 as the master board that will take care of the clock for other TURBO boards, which
 201 act as slaves.

202 A LabView program can be used to control TURBO boards remotely. This pro-
 203 gram can perform standard threshold and latency calibration scans. Further, it can
 204 also be used for data acquisition and quality control tests.

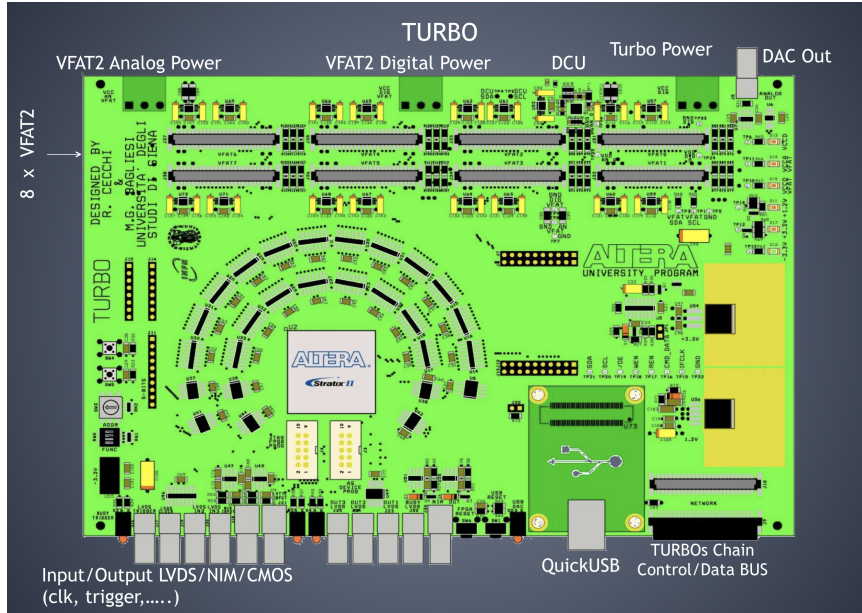


Figure 1.10: TURBO board [15].

205 Measurement Mode

206 Data can be collected in two different modes: synchronous mode and asynchronous
 207 mode. In the asynchronous mode, triggers are not correlated with the clock while
 208 in a synchronous mode triggers are correlated with the leading edge of the LHC 40
 209 *MHz* clock. Synchronous mode is used to collect data in sync with the LHC clock.

210 1.3.3 Beam Test Experimental Set-up

211 The experimental set-up consists of three plastic organic scintillators, three trackers
 212 and a GE1/1 prototype, being flushed with an Ar/CO₂ (70:30) gas mixture. The
 213 trackers are triple-GEM detectors with an active area of 10 cm × 10 cm having 256
 214 strips in both horizontal (y-coordinate) and vertical (x-coordinate) directions with
 215 respect to the beam and a pitch of 0.4 mm. The three trackers constitute a muon
 216 tracking telescope which is used to reconstruct the beam trajectories and reduces
 217 background events. Figure 1.11 shows the experimental set-up used to perform beam

218 test studies. The GE1/1 prototypes are installed on a movable table to scan different
 219 sectors. At a time only one ($\eta, i\phi$) sector of GEM detector is irradiated with the beam.
 220 The CMS test chamber was placed, close to the tracking hodoscope, on a vertically
 221 movable support to allow scanning. The scanned sectors of the GE1/1 detector are
 222 shown in Fig. 1.13.

223 The tracking telescope is equipped with the digital chips VFAT2 [16], which pro-
 224 vides a binary output with a variable latency for the position information and a fixed
 225 latency output, called SBIT, for the timing information.

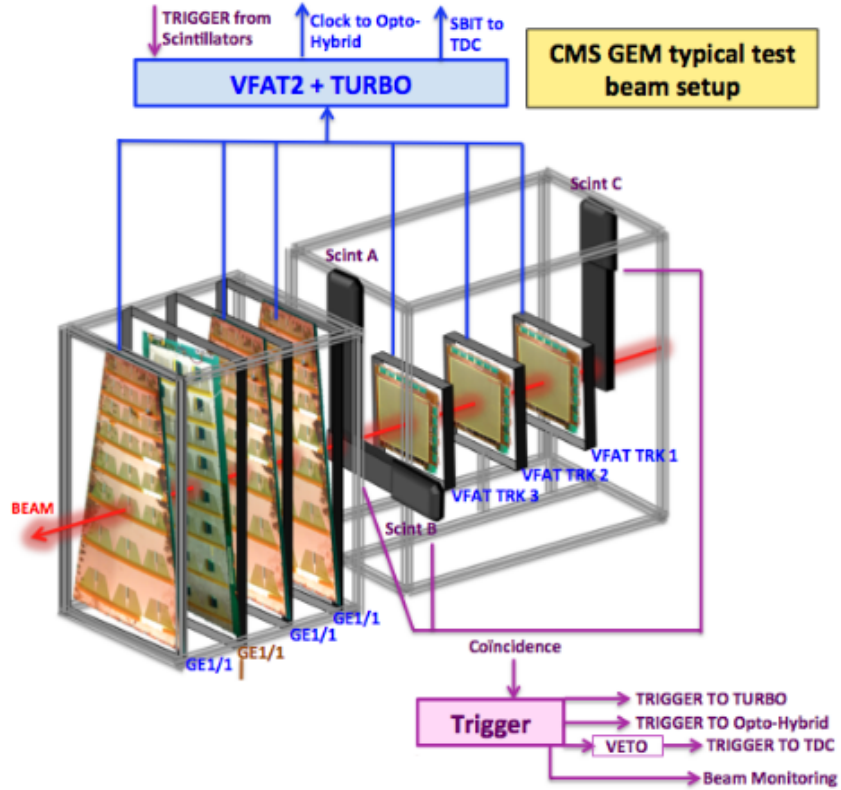


Figure 1.11: Schematic view of the beam test set-up with the three tracking GEM detectors and a GE1/1 prototype.

226 On detector electronics connects the output from the front-end ASIC (VFAT2) to
 227 the GEM readout board. The VFAT2 chip is connected to the hybrids which are

228 plugged into the connectors on the readout board. The analog pulses from the three
 229 scintillators, named S1, S2 and S3 are fed into discriminator for analog to digital
 230 conversion. The discriminator output was provided into the logic coincidence (to
 generate event trigger) before being sent to the other DAQ systems (Figure. 1.12).

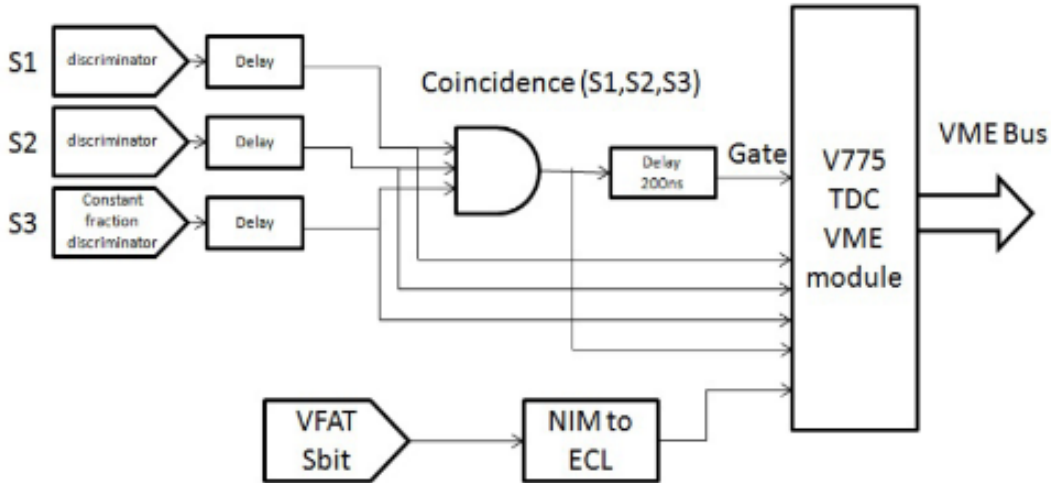


Figure 1.12: Perspective view of the experimental set-up used for performance measurement in the beam test studies. The trigger system is generated using the signal collected from three scintillators connected in coincidence.

231

232 1.3.4 Data Analysis

233 The raw data collected during these beam test campaigns were in binary format.
 234 First, the raw data (binary information) is converted into the ROOT data format.
 235 “**TURBO-SOFTWARE**” [17] package is used for data analysis framework. Orig-
 236 inally developed by TOTEM group, it is used to perform this task. The output from
 237 TURBO-SOFTWARE data analysis consists of hit information for each strip from
 238 the detectors which are further used to reconstruct the particle tracks and clusters.
 239 A **hit** is defined when one or more strip of the VFAT chips surpass the threshold
 240 set on the readout chip. A **cluster** is defined as the number of adjacent fired strips

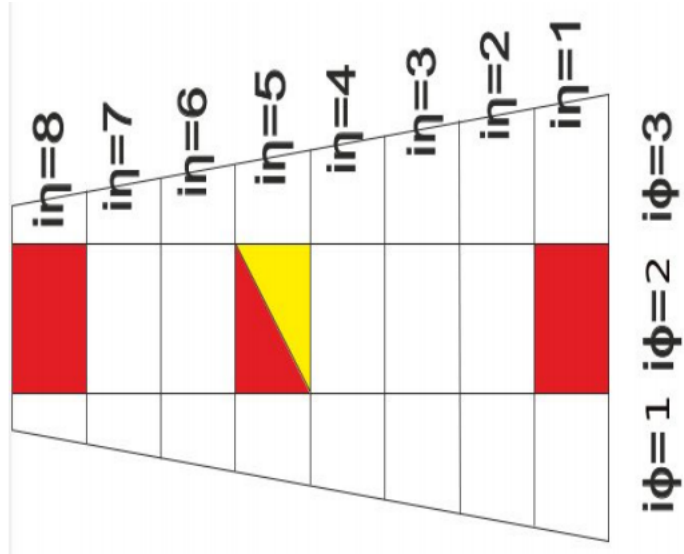


Figure 1.13: Different $(i\eta, i\phi)$ sectors of a full-size GE1/1 detector prototype. The red and yellow colour shows which sector of GE1/1 is exposed to the beam. Red sectors are collected with $Ar/CO_2/CF_4$ (45/15/40) gas mixture while the yellow sectors are taken with Ar/CO_2 (70/30) gas mixture.

241 along x or y-axis. The first step towards the track and cluster reconstruction is to
 242 discriminate the background tracks coming from detector noise (fake tracks) from the
 243 signal (muon) tracks. Once the fake tracks are removed from the collection, valid hits
 244 are used to generate tracks.

245 The hit profile and beam profile recorded in the tracker for one of the runs are
 246 shown in Fig. 1.14 and 1.15. From both hit profile and beam profile, one can see
 247 that the beam is point beam like a beam having a Gaussian spread, centred around
 248 (50,50), i.e., at the centre of the tracker.

249 This sorting is done by selecting events having only one cluster in each tracker.
 250 The cluster positions are fitted using a polynomial fit of order one and χ^2 of the fit
 251 is recorded. The event is discarded if the χ^2 of the fit is greater than 10.

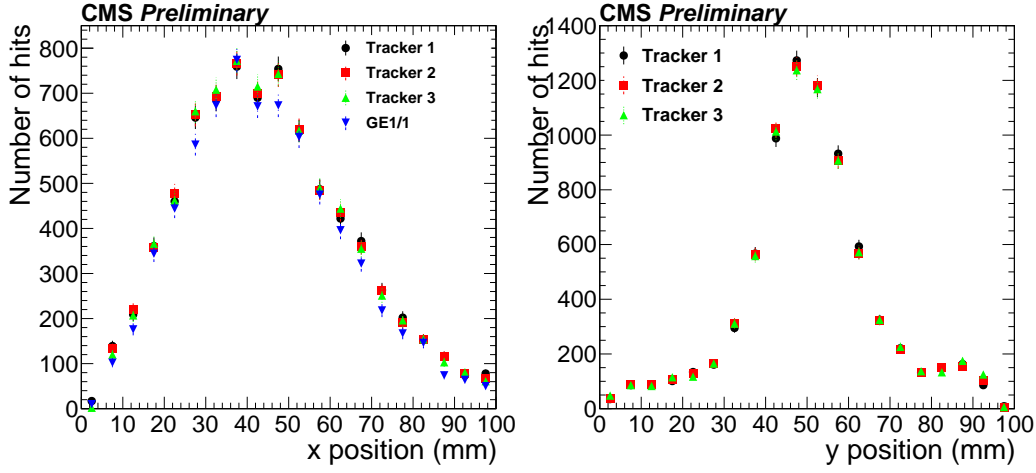


Figure 1.14: Tracker hit distribution along x and y axis and GE1/1 hit distribution along y. This is plotted from one of the runs taken during test-beam.

252 Detector alignment studies

253 Detector alignment is one of the core parts of the data analysis. For the efficient track
 254 reconstruction and for good tracking efficiency, it is necessary to align the detectors.
 255 Detectors can be aligned manually (online) and offline is software based. During the
 256 beam test, the trackers and GE1/1's are aligned manually. Thus, one can achieve
 257 precession of up to few centimetres only. Thus, it is always important to check
 258 the detector alignment using the software to achieve better efficiencies and spatial
 259 resolution.

260 The technique used for this purpose consists of the interposition along the trajec-
 261 tory of several detector planes where the particles pass through; from the interpolation
 262 of all these points can be reconstructed the trajectories followed by the particles. In
 263 these environments one of the most important figures of merit of the detectors is
 264 the spatial resolution, that is the capability to reconstruct the crossing point of the
 265 particle. The goal is to reduce the χ^2 of the track fits in order to improve track and
 266 quality eliminating or reducing bias in the detector data.

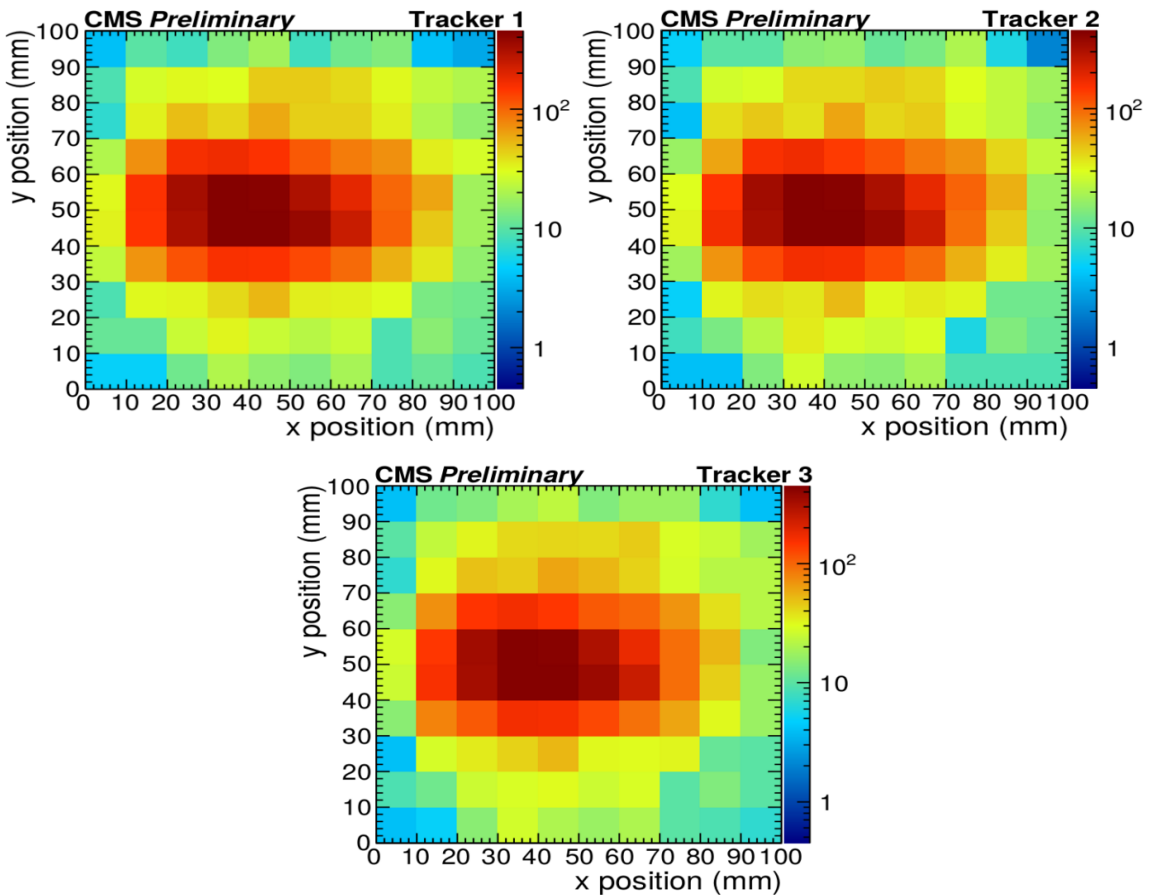


Figure 1.15: 2D- beam profile plot for the first, second and third tracker. The X and Y axis of the plots correspond to the distance (in mm) measured from the central position of the trackers in X and Y direction respectively. The different colors in the color palette correspond to the number of hits registered in the detector at a particular (x,y) position.

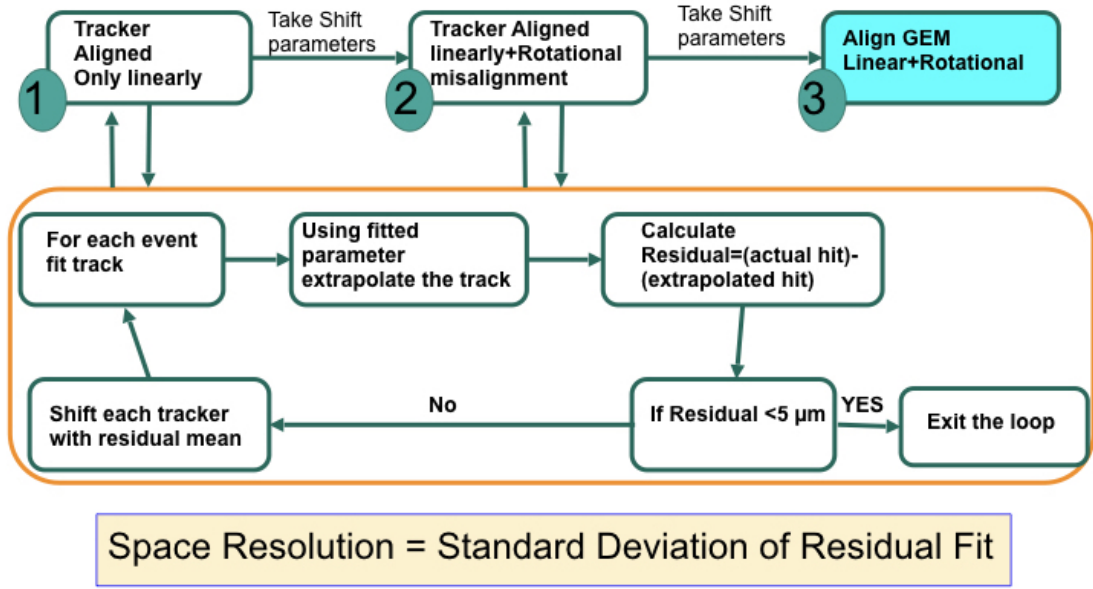
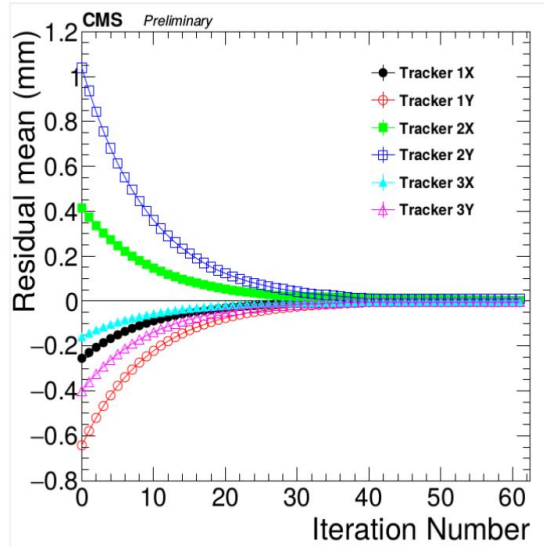


Figure 1.16: Flowchart illustrating the workflow of detector alignment algorithm.

267 Linear and Rotational Alignment

268 To measure the spatial resolution of GE1/1 detectors, these detectors aligned with
 269 respect to the tracker system. This starts with the need to be mutual alignment of the
 270 three tracking detectors that have 2-D readout in the Cartesian coordinate system.
 271 The first alignment step is to shift each of the three tracking detectors iteratively in
 272 the XY-plane to make their origins coincide in the same line of sight. The initial
 273 shift parameters are the mean values from the position distributions of X and Y axis.
 274 During each iteration, a linear fit is performed to the hits position along X and Y
 275 direction from each tracker. Residuals are histogrammed for every detector and their
 276 distributions are fitted with a double-Gaussian function. Ten percent of the residual
 277 mean value of each detector is taken as the shift parameter in the next iteration to
 278 avoid overcorrection. This step is repeated until the resulting residual mean value
 279 converge towards zero. This method provides a first coarse alignment. In the second
 280 alignment step, we correct also for relative rotations of the tracking detectors around

281 the beam axis in the XY-plane. We again fit straight lines to the hit in X and Y
 282 direction and iterate through a succession of offsets and rotations around the beam
 283 axis relative to the first tracking detector. Again this process is repeated until the
 284 residual means from the trackers are very close to zero and χ^2 of the track fits is
 285 also observed at each iteration. In each iteration, the detectors are first shifted and
 286 then rotated; then new residuals and rotation angles are calculated. This process is
 287 repeated iteratively until the residual means from the track fits become less than 0.005
 288 mm. Fig. 1.16 shows the flow chart of the alignment algorithm. Figure. 1.17 shows
 289 the variation of track residuals for three trackers as a function of iteration number,
 with residual shifting to lower values progressively through iterations.



22

Figure 1.17: Variation of track residuals for three trackers with respect to the iteration number

290

291 Alignment of GEM detectors w.r.t Reference Tracker

292 Once the tracker alignment, the next step is to align trapezoidal GEM detectors with
 293 respect to the centre of the aligned tracker system. A twofold iteration loop is used

294 wherein the x-offset is kept fixed the y-offset is iterated over a set of values with a
295 small iteration step. The x-offset is also iterated over and corresponding to every
296 single value of x-offset, the y-offset are iterated. For each value of (X offset, Y offset)
297 pair, tracks are linearly fitted in the ϕ co-ordinate and the corresponding residuals
298 are noted and used to align the detectors.

299 Fiducial Area Selection

300 To have an efficient efficiency we should also define a fiducial area in which we are
301 going to calculate the efficiency. We define the fiducial area as:

- 302 • Only valid tracks are considered during this procedure, which are defined as the
303 tracks having hits registered in all the three trackers.
- 304 • These valid tracks are then extrapolated to GE1/1's. Only those tracks are
305 finally selected for which the corresponding hit position in the GE1/1 has a
306 residual value less than 5mm.
- 307 • The selected events are used to fill 2D histogram for different cases. The first
308 histogram contains all those events that have a valid hit in the trackers only, as
309 shown in Fig. 1.18 (left). Another 2D histogram is filled with all those events
310 where there are valid hits in all three trackers as well as in the GE1/1, as shown
311 in Fig. 1.18(right). The ratio of the two histograms defined above is computed
312 and is shown in Fig. 1.18 (bottom)
- 313 • Finally, the region (0,80) in the ratio histogram where efficiency is maximum is
314 considered as the fiducial region. This fiducial region is used for the efficiency
315 calculation for GE1/1 detector.

³¹⁶ Here, the calculated fiducial region is (0,80), which can be observed from Fig. 1.18(bottom).

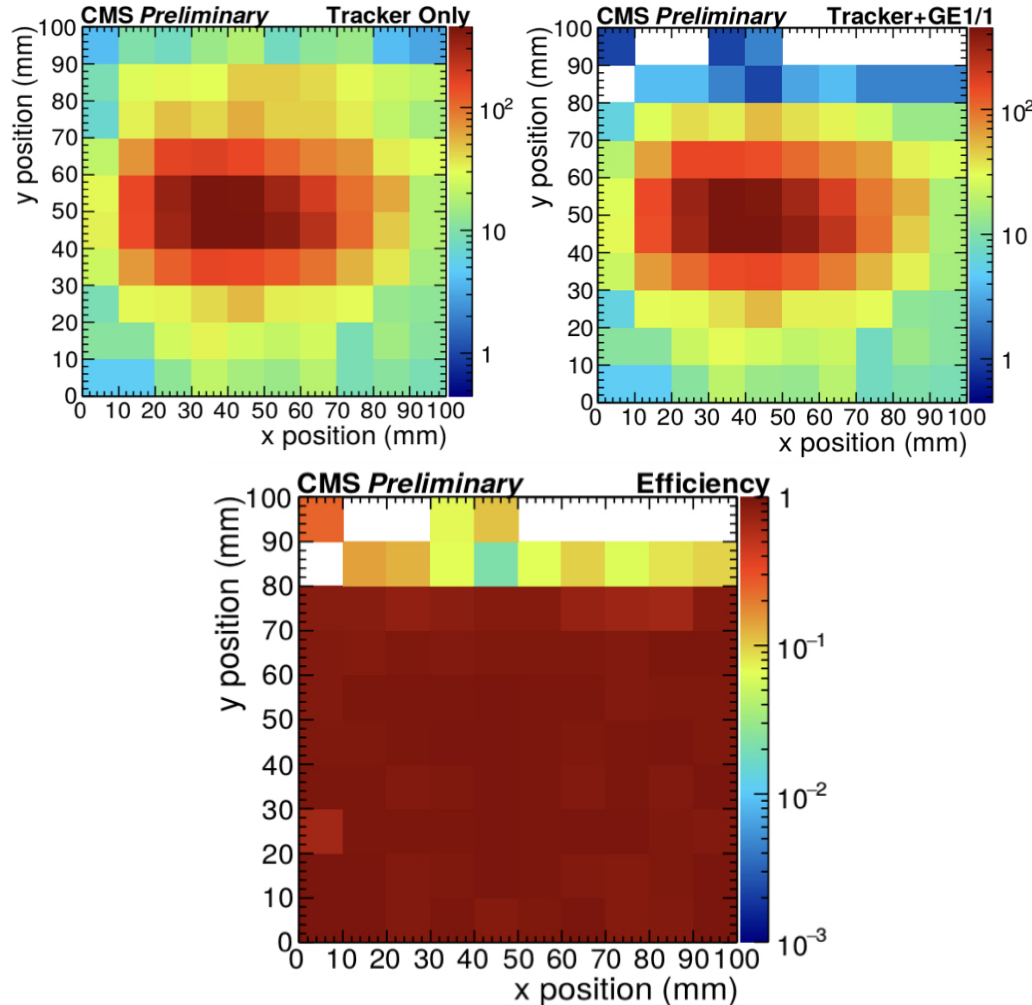


Figure 1.18: 2D distributions showing events with hits registered in the trackers (top left), events registered in three trackers and GE1/1's (top right) and the division of the two histograms used to define the fiducial region for GE1/1 efficiency measurements (bottom).

318 **Efficiency Measurement**

Efficiency, ϵ , for a GE1/1 detector for the current beam test set-up is defined as:

$$\epsilon = \frac{N_{GE1/1+Trk}}{N_{Trk}} \quad (1.2)$$

where N_{Trk} is the number of reconstructed events with hits reconstructed in the three trackers and $N_{GE1/1+Trk}$ is the number of reconstructed events for which an actual hit is also found in the GE1/1 detector. Detector efficiency is calculated as a function of current supplied to the high-voltage divider as well as E_{gain} is shown in Fig. D.3

where E_{gain} is defined as

$$E_{gain} = \frac{I \times R_{avg}^{gap}}{D} \quad (1.3)$$

where I is current supplied to the HV divider, R_{avg}^{gap} is the average gap resistance of GE1/1, and D is thickness of the GEM foil. Here, the efficiency is fitted with the function defined as:

$$\epsilon = \frac{\epsilon_{max}}{1 + e^{s(HV - HV_{50\%})}} \quad (1.4)$$

319 Where, ϵ_{max} is the maximum obtained efficiency, $HV_{50\%}$ is the applied HV (or current
320 or E_{gain}) at which the efficiency is 50% and s is just a scale factor left floating for fit
321 to determine. The fit parameters are shown in appendix D.

322 Fig. D.3 shows the GE1/1 detection efficiency with two different gas mixtures
323 Ar/CO_2 (70/30) calculated for sector $(i\eta, i\phi) = (5, 2)$ and $Ar/CO_2/CF_4$ (45/15/40)
324 for three different sectors $(i\eta, i\phi) = \{(1, 2), (5, 2), (8, 2)\}$. We achieved a very good
325 efficiency of $\sim 98\%$ in all cases. It should be noted that the efficiency curves for
326 different gas mixture do not coincide because for a given high voltage operating
327 point, the effective gain of detector with Ar/CO_2 mixture is approximately one order
328 of magnitude higher than that for the $Ar/CO_2/CF_4$ mixture. This implies that we

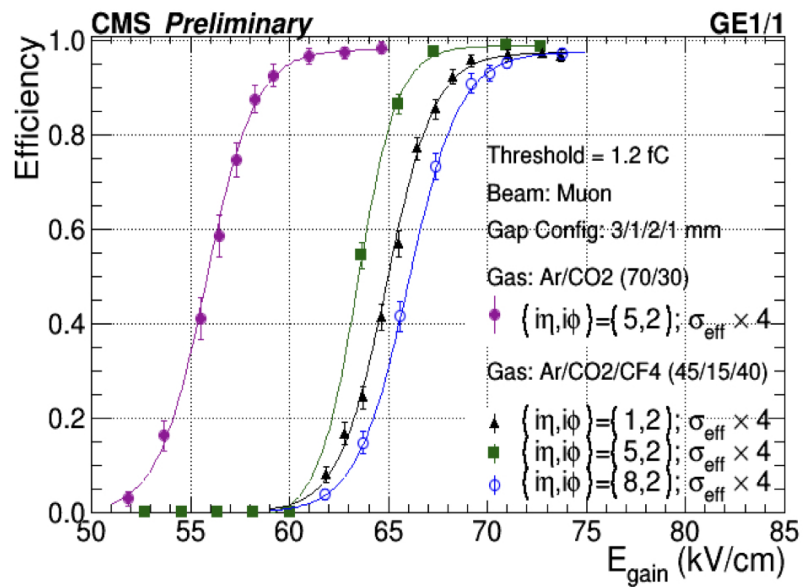
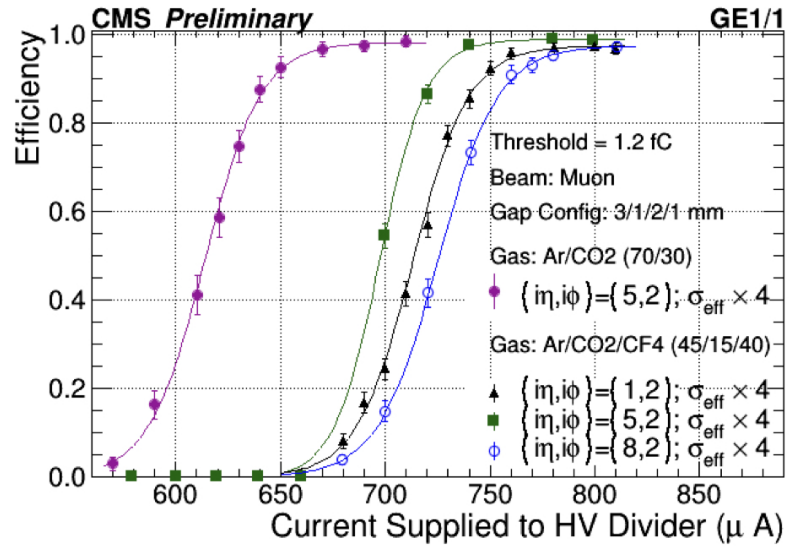


Figure 1.19: Efficiency with respect to E_{gain} for two different gases and three different $(i\eta, i\phi)$ sectors.

329 can operate our detector without using CF_4 gas, which is non-eco friendly, without
330 compromising with the efficiency.

331 **Time Resolution**

The time resolution is defined as the time taken by detector to generate a signal on the readout electrode after the passage of particle through it. Experimentally, the time resolution is the root-mean-square of the Gaussian distribution of the time taken by the particle to reach detector from the scintillator. The detector time response is modelled as the Gaussian function, $f(t)$, convoluted with a square wave, $g(t)$, having a pulse length $f_{clk} = 25\text{ns}$ (LHC clock frequency) to represent discrete sampling. The functions $f(t)$ is given by:

$$f(t) = Ae^{-\frac{1}{2}\left(\frac{t-t_0}{\sigma}\right)^2} \quad (1.5)$$

where A is amplitude of Gaussian function, t_0 is the mean value of Gaussian, and σ is the standard deviation of Gaussian. And, $g(t)$ is given by

$$g(t) = \begin{cases} 0, & \text{else} \\ 1, & -\frac{f_{clk}}{2} < t < \frac{f_{clk}}{2} \end{cases} \quad (1.6)$$

where, f_{clk} is the length of created 40MHz window. The convolution of the two functions is given as

$$(f * g)(t) = A \cdot \sigma \sqrt{\frac{\pi}{2}} \left(\operatorname{erf}\left(\frac{u_+}{\sigma\sqrt{2}}\right) - \operatorname{erf}\left(\frac{u_-}{\sigma\sqrt{2}}\right) \right) \quad (1.7)$$

332 where, $u_{\pm} = t - t_0 \pm \frac{f_{clk}}{2}$. The the experimental data is fitted with this convoluted
333 function. The extracted time resolution as a function of E_{drift} and current supplied
334 to high voltage divider are shown in Fig. 1.20.

335 Here, the time resolution for the detector operated using gas Ar/CO_2 gas mixture
336 is fitted using a polynomial of degree 2, while the one with $Ar/CO_2/CF_4$ gas mixture
337 was fitted using the polynomial of order 6. Also, the fit parameters for each fit is
338 given in appendix D.

339 The time resolution with Ar/CO_2 (70/30) is higher for lower values of E_{drift} . This
340 means that we are able to reach faster timing at lower gains with addition of CF_4
341 and it is important from the point of view of detector safety because this will allow
342 us to operate the detector at lower gains, hence reducing the discharge probability.

343 Cluster Size Measurement

344 To measure the cluster size of GE1/1, clusterization algorithm is used. The basis
345 of this algorithm is that we consider clusters if one or more continuous strips in
346 GE1/1 are fired. Three golden run ranges, with different pseudo-rapidity sectors, viz
347 2014H4A, 2014H4C and 2014H4D are studied. The description of these runs is given
348 in Table 1.1.

349 To fit the cluster size distribution, Poisson function is used. Figure 1.21 shows the
350 cluster size distribution for different (η, ϕ) sector fitted using the Poisson distribution
351 function.

352 Distribution is studied for different values of fiducial region and it is observed that
353 the cluster size is independent of the fiducial region (Fig. 1.22).

354 Cluster size study distributions for the GE1/1-IV and GE1/1-IV-GIF are plotted as
355 a function of current supplied to the high voltage divider and are shown in Figure 1.23.
356 The cluster size is greater in $(\eta, \phi) = (5,2)$ region for both the detectors due to
357 the uniformity in readouts channels. As it is known that the GE1/1 4th generation
358 prototype is suffered from the significant bending in the readout and drift PCB. This
359 impacts GE1/1 properties like primary charge created, uniformity, transparency of

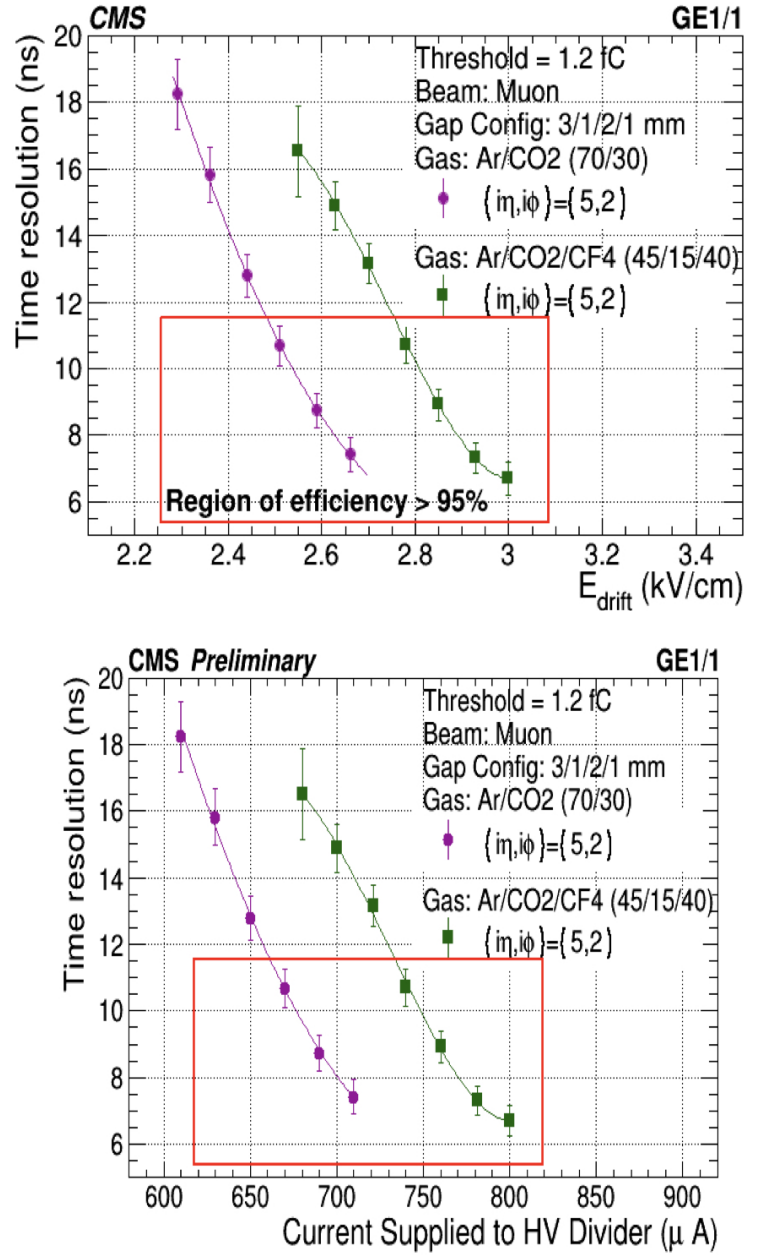


Figure 1.20: Time-resolution with respect to E_{drift} (top) and current supplied to high voltage divider (bottom) for two different gas mixture.

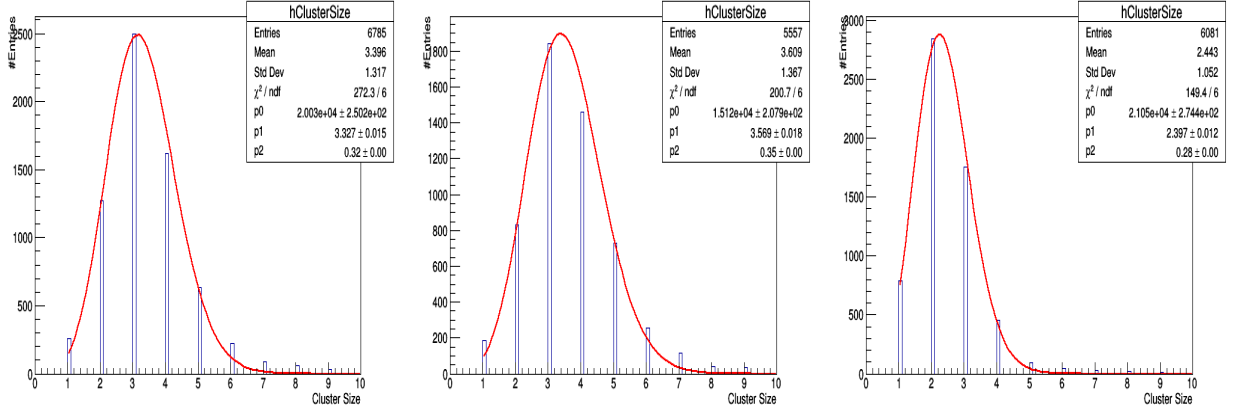


Figure 1.21: Cluster size distribution for GE1/1 detectors obtained during the beam test campaign: for run number 1644 in region $(\eta, \phi) = (5,2)$ (left), for the Run number 1869 in region $(\eta, \phi) = (8,2)$ (middle) and for Run number 2066 in region $(\eta, \phi) = (1,2)$ (right).

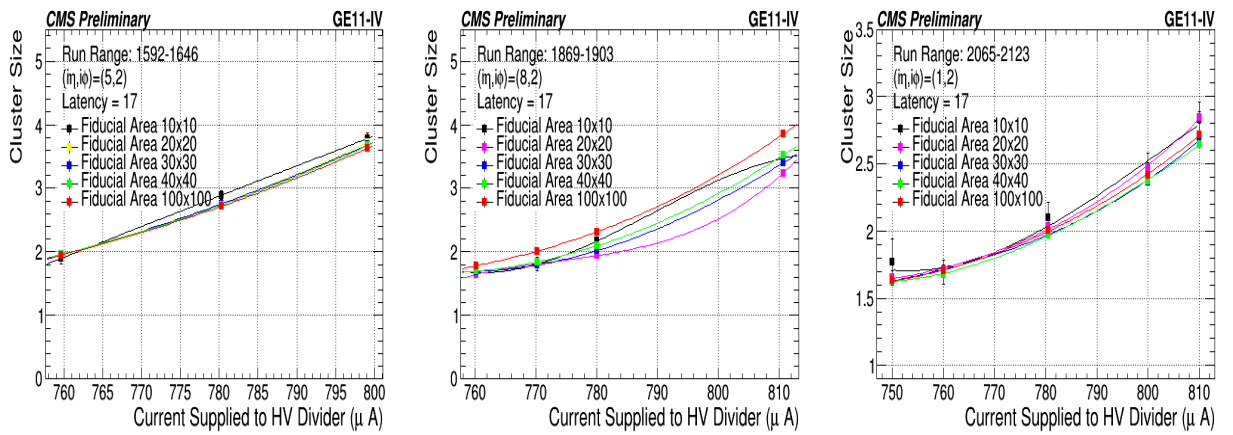


Figure 1.22: Mean value of cluster size distribution at different current supplied to high voltage divider obtained during the beam test campaign: for 2014H4A which was taken for region $(\eta, \phi) = (5,2)$ (left), for 2014H4C taken for region $(\eta, \phi) = (8,2)$ (middle) and for 2014H4D taken for region $(\eta, \phi) = (1,2)$.

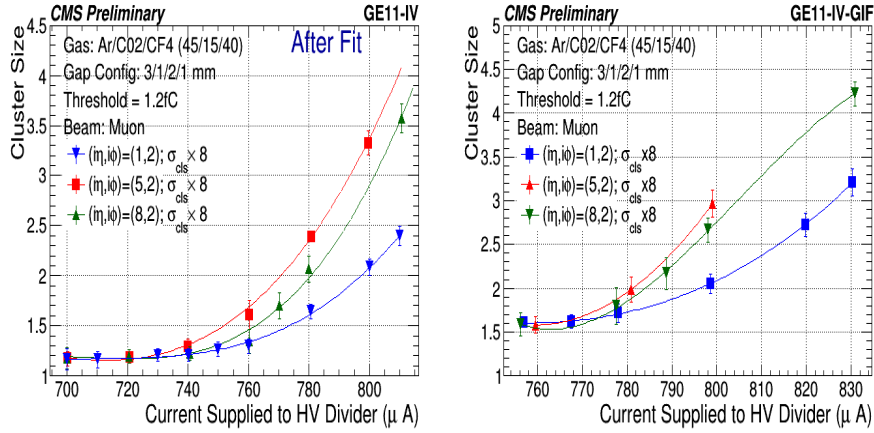


Figure 1.23: Cluster size distribution: Left - GE1/1-IV, Right - GE1/1-IV-GIF

bottom of third GEM foil, charge collection by the readout, etc. Thus, it is expected that that non-uniformity in the cluster size distribution in (η, ϕ) sector (1,2), (5,2), and (8,2) is because of this. This issue is improved in the next version of GE1/1 prototype, known as GE1/1-V.

1.4 Characterization and Production of GEM Foil

Through the Transfer of Technology (TOT) agreement with CERN, Micropack Pvt. Ltd. (a Bangalore based company) signed an agreement for the development of GEM foil in India in association with the Indian institutions. Micropack started producing the 10 cm \times 10 cm GEM foils using the single mask technique, as being used to produce GEM foils for GE1/1 detectors. Soon it was realized that the production of GEM foil using the single mask technique is quite challenging and thus switched to the double mask production technique. Same production technique were adopted for the foil production as being done at the CERN PCB workshop [18].

Micropack used the Kapton foil having a thickness of 50 μm with 5 μm of copper

³⁷⁴ coating on its either sides. Fig. 1.24a shows the $10\text{ cm} \times 10\text{ cm}$ GEM foil produced
³⁷⁵ by Micropack and the cross-sectional view of its double conical hole is shown in
Fig. 1.24b.

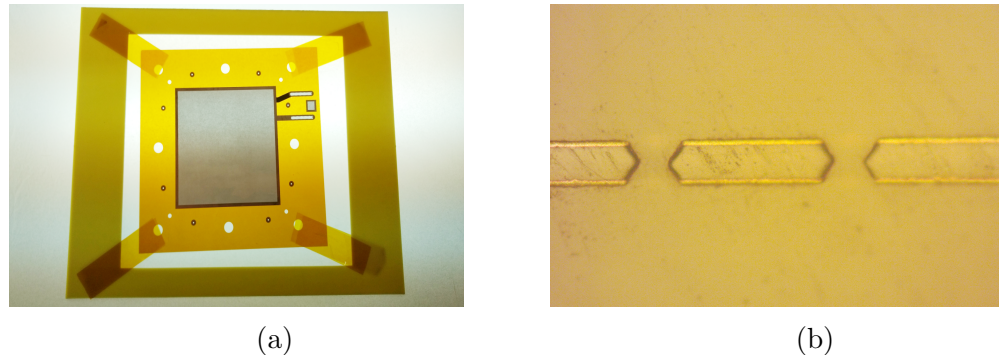


Figure 1.24: (a) $10\text{ cm} \times 10\text{ cm}$ GEM foil encapsulated in a frame and (b) Cross-sectional view of the foil showing the double cone structure of the engraved holes, developed by Micropack.

³⁷⁶
³⁷⁷ Before being used for the detector fabrication, the GEM foils required to pass
³⁷⁸ certain quality control tests, which are listed below:

³⁷⁹ 1. Visual inspection

³⁸⁰ 2. Optical test, and

³⁸¹ 3. Electrical test

³⁸² All these tests are required to be performed in the clean room⁵ of at least class 1000
³⁸³ or better. This is done to avoid the filling up of GEM foils with dust particles. Even
³⁸⁴ a small amount of dust inside the GEM holes could lead to a destructive discharge
³⁸⁵ thereby destroys the whole foil. At Delhi University the GEM foils are handled in the
³⁸⁶ clean room of class 100. It is installed with KANOMAX dust particle counter model

⁵Clean room is a specially designed room, maintained at extremely low level of particles per cubic meters, for a specialized industrial production or scientific research. For example, a “Class-100” clean room is designed to never allow more than 100 particles (0.5 microns or larger) per cubic foot of air. “Class-1000” and “Class-10000” clean rooms are designed to limit particles to 1000 and 10,000 respectively.

³⁸⁷ 3887 [19] which continuously monitors the particle count inside the clean room. Also,
³⁸⁸ the clean room is equipped with a dehumidifier for humidity control.

³⁸⁹ 1.4.1 Visual Inspection

³⁹⁰ At first one has to inspect visually the GEM foil for any dust or defects visible to the
³⁹¹ naked eye. GEM foils are cleaned using the adhesive rolled as shown in Fig. 1.25 to
remove dust particles.



Figure 1.25: Adhesive roller used for the cleaning of GEM foil.

³⁹²

³⁹³ 1.4.2 Optical Test

³⁹⁴ Optical test is carried out to check the GEM foil for any:

- ³⁹⁵
- microscopic defects, not visible to the eyes and
 - to measure the inner and outer hole diameter and the pitch size.

³⁹⁷ The motivation to perform the optical test is following:

- ³⁹⁸
- The foil defects such as the over-size hole, missing hole, excess etching, etc could
³⁹⁹ degrade the performance of foil and thus the overall detector efficiency.

- 400 • As the gain of the detector depends on the diameter of the hole and thickness of
 401 the foil (as shown in Fig. 1.26). Thus, it is necessary to check their dimensions.

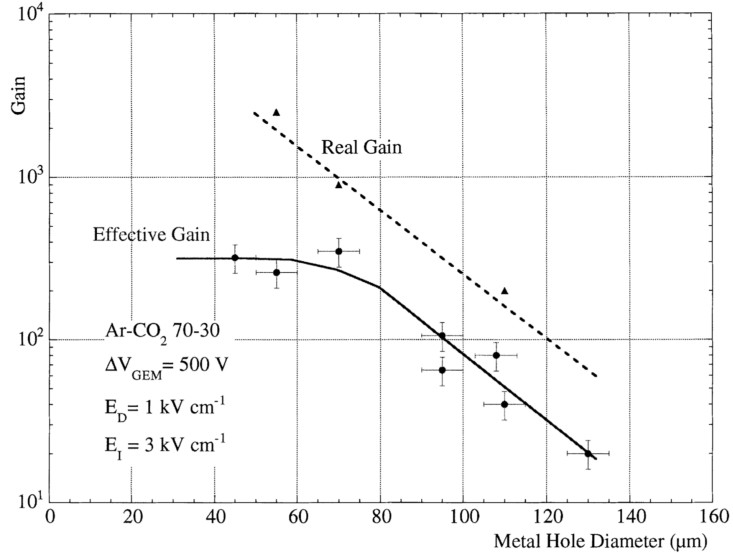


Figure 1.26: Real gain and effective gain variation with GEM hole diameter [20] having a foil thickness of $60 \mu m$ ($= 50 \mu m + 5\mu m + 5 \mu m$). As the hole diameter decreases, the effective gain increases till $70 \mu m$ and after that it reaches saturation. This is due to loss of generated electrons in the avalanche to the bottom of the GEM electrode when hole diameter is reduced below the foil thickness.

- 402 To check any defects and to measure the hole-size and pitch for a GEM foil several
 403 methods have been developed using an automated 2D-CCD scanner [21, 22]. However,
 404 we used a different technique. We divided the GEM foil into several sectors and
 405 captured a high-resolution picture using the AF-S Micro Nikon 40 mm 1:2.8G lens.
 406 We used a softbox ($1 m \times 1 m$) light source for uniformly illuminating the GEM foil.
 407 A sketch of the set-up is shown in Fig. 1.27. Fig 1.28 shows the found defects in the
 408 considered GEM foil. Also, the observed number of defects are shown in Fig. 1.29.
 409 Out of 600,000 holes in the GEM foil, defects were found in 785 holes, i.e, 0.13% of
 410 total holes are defected. Also, similar number of defects were observed in other two
 411 GEM foils. The resulting local effects in the GEM foil due to these small fractions of

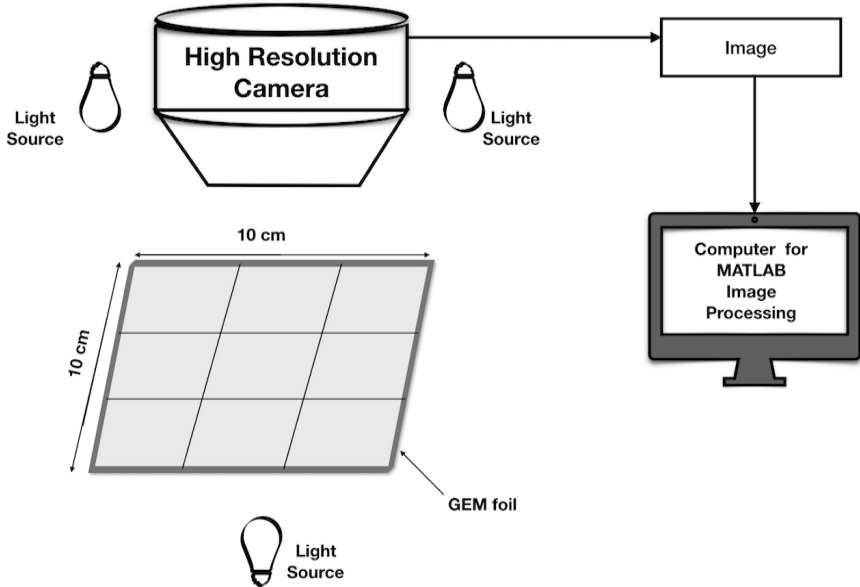


Figure 1.27: Sketch of the set-up used for optical measurements of the GEM foil.

⁴¹² defected holes are not expected to deteriorate the overall performance of the GEM detector.

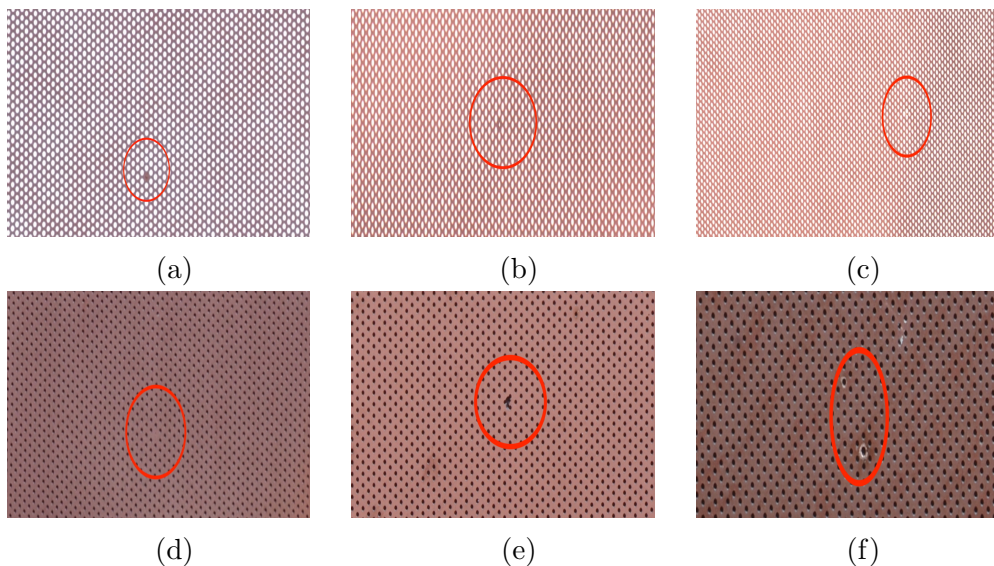


Figure 1.28: Observed imperfections in the GEM foils: (a) Un-etched area, (b) under-size hole, (c) over-size hole (d) missing hole, (e) excess etching and (f) burnt area.

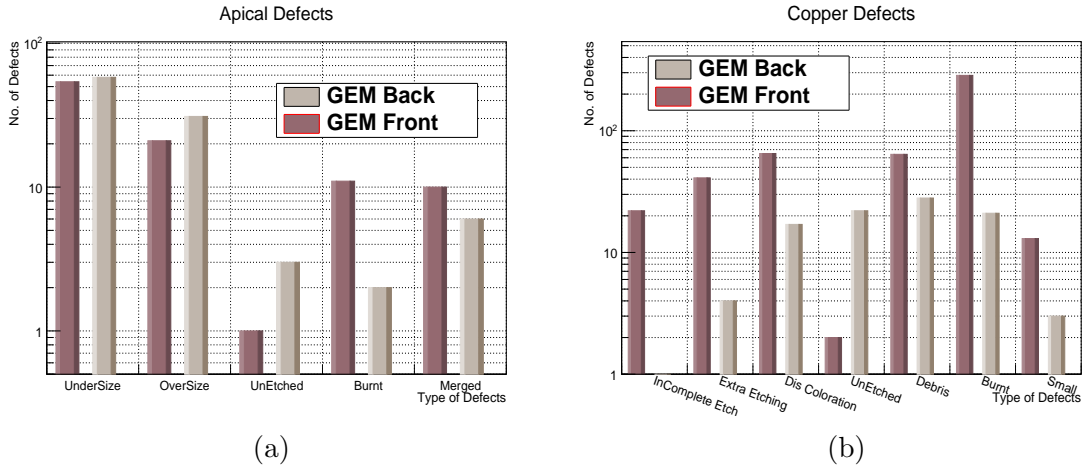


Figure 1.29: Number of defects seen in (a) Insulator (Apical Type NP) and (b) Copper, for one of the 10 cm × 10 cm foil.

414 1.4.3 Electrical Test

415 This is one of the most important tests for the GEM foil, which deals with the
 416 measurement of leakage or dark current. Dark current exceeding the prescribed limits
 417 could lead to a short circuit in the foil thereby damaging the foil permanently. A spark
 418 can also be produced due to presence of dust particle on the GEM foil, hence, the
 419 cleanliness of GEM foils is also ensured during this test. But, if a huge number of
 420 frequent sparks happen then we should quickly stop the electricity and clean the foil
 421 properly. The electricity test are carried out for foils in two steps as per the CERN
 422 standards [23]:

423 1. Quality control fast or QC-fast and

424 2. Quality control for long or QC-long.

425 QC-long and QC-short tests differ in terms of the duration for which high voltage
 426 is applied to the detector to monitor its leakage current. Other difference is that
 427 QC-fast gives us a quick result about the leakage current or electrical connectivity of

428 the foils while QC long provides the behaviour of foil at high voltages and gives us
429 the actual leakage current and the number of discharges if present.

430 **QC-fast**

431 This test is performed using the insulation tester MIT Megger 420 [24]. This test
432 confirms that the foil have good electrical connectivity. As 550 V potential is applied
433 across the GEM foil for about a minute, current does not exceed 10 nA and the
434 resistivity in the air between the two foils exceeds $2 G\Omega$.

435 **QC-long**

436 For this, the measurement the electronics set-up is shown in Fig. 1.30. It consists of
437 a GEM foil enclosed in a Plexiglass enclosure in which nitrogen gas is continuously
438 floated. The foil was connected to a the Keithley 6517B picoammeter [25] interfaced
439 with a computer via a GPIB interface and the LabView program is used to record the
440 measurements. The leakage current is measured as a function of applied voltage as
441 shown in Fig. 1.31a. Also, for the sake of comparison same measurement was made
442 with 10 $cm \times 10 cm$ GEM foil produced at CERN. The results using the CERN foil
443 are shown in Fig. 1.31b. It is observed that the two foils - one produced by Micropack
444 and another produced at CERN - show similar behaviour and the leakage currents
445 are well within the limit (10 nA), set by CERN QC criteria.

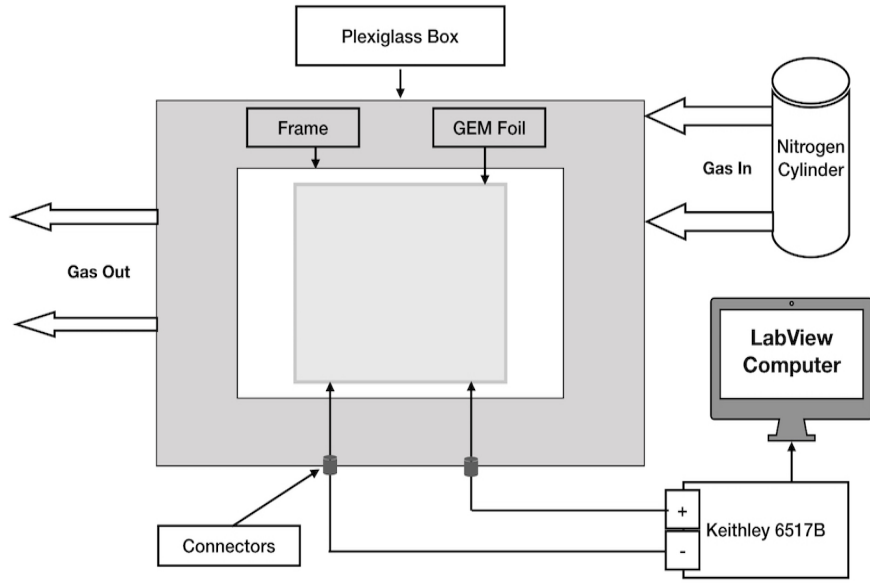


Figure 1.30: Sketch of the set-up used for the measurement of leakage current.

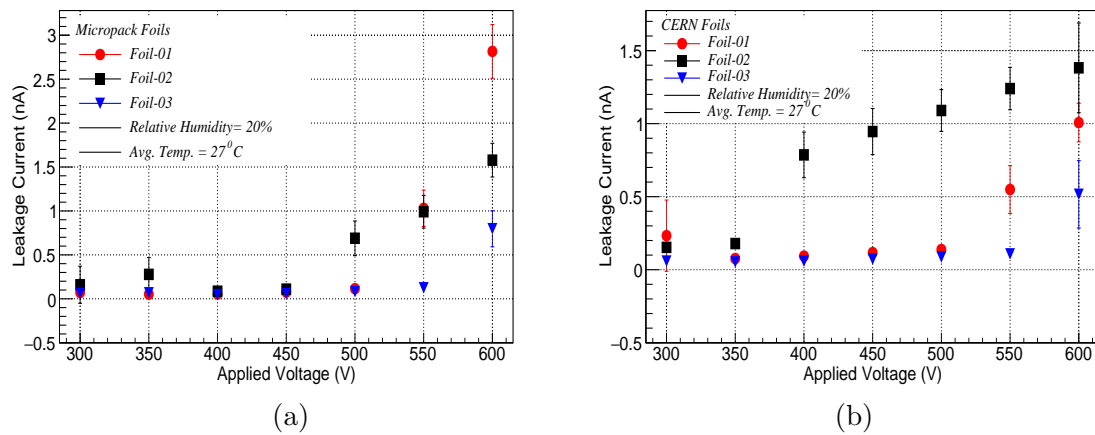


Figure 1.31: Leakage Current for (a) Micropack Foils and (b) CERN Foils, at an average temperature of $T=27^\circ \text{C}$ and 20% relative humidity.

Appendices

446

⁴⁴⁷ **Appendix A**

⁴⁴⁸ **GE11 detector generations**

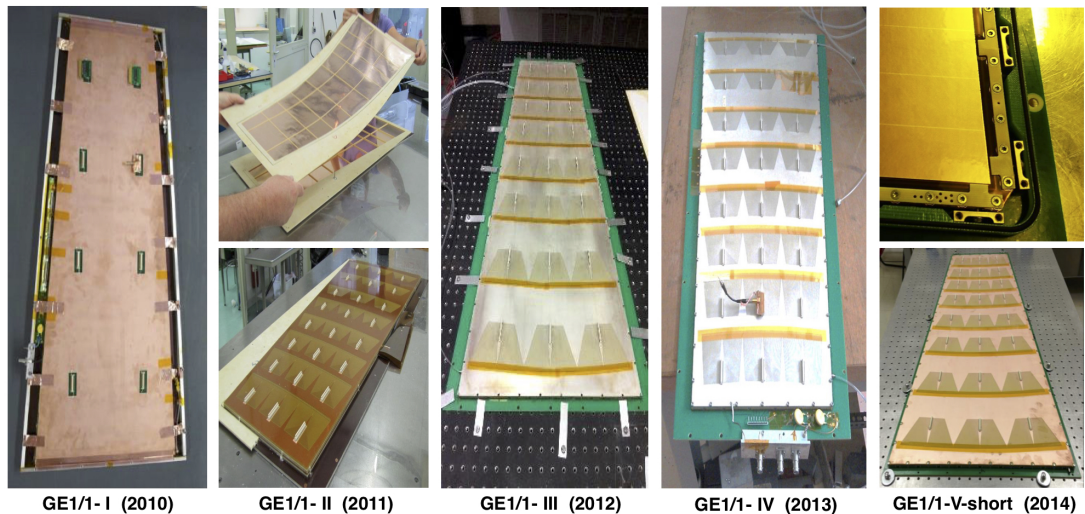


Figure A.1: Five different generations of GE11 detector developed and improved with time.

⁴⁴⁹ From 2010 till now total of five different GE11 versions are developed and tested
⁴⁵⁰ every year. Based on the experience every new generation was improved from its
⁴⁵¹ previous versions.

⁴⁵² In the first version of GE11, GE11-I, prototype was build 1m-class GEM detector

453 and operated. In this detector different components are glued together and to have
454 gaps between different GEMs spacer ribs were used to have the gap configurations
455 3/2/2/2 mm. In this version total 8 readout sector was there [26].

456 In the next version, GE11-II, the readout sectors were increased from 8 to 24 which
457 are arranged as 8- η partitions and 3- ϕ partition (columns). Here, each η partitions
458 had 384 radial strips with 455 μrad angular pitch. Also, to speed up the signal, the
459 foil gap configurations are changed to 3/1/2/1 mm [27].

460 In the third version of GE11, known as GE11-III. In this version it was split into
461 several pieces and used the mechanical stretching during the assembly then glued to
462 the frame and drift board [28].

463 In the fourth version of GE11, GE11-IV, the major achievement was to abandoned
464 the use of glue while assembling the detector. Because of this the stretching improved
465 and the board deformation issue was resolved as compared to the GE11-III. Still it
466 takes few hour in assembling and need to use the pre-bending of the with respect to
467 the bowing observed. Thus, it was not reliable for the mass production [29].

468 The pre-bending issue is resolved in the GE11-V prototype by tensioning the foil
469 against the independent “pull-out” pieces. This version is opted for the final produc-
470 tion of the GE11 chamber for installation in the CMS during Long-Shut-down-2.

⁴⁷¹ **Appendix B**

⁴⁷² **Gaseous Detector Important**
⁴⁷³ **Points**

⁴⁷⁴ **B.1 Gain Measurement**

The gain of a detector can be calculated using the ratio of output to the input value of current, like:

$$Gain = \frac{I_{out}}{q \times f} \quad (B.1)$$

where q is the charge collected at the first layer of GEM foil and is calculated as:

$$q = n \times e \quad (B.2)$$

⁴⁷⁵ where e is the electron charge, n is the average number of electrons produced in the
⁴⁷⁶ drift region by the incident particles and f is the interaction rate of the incident
⁴⁷⁷ particles in the gas. For the given X-ray source with a specific energy and the known
⁴⁷⁸ ionization potential of the used gas mixture n can be calculated and in our case it is
⁴⁷⁹ found to be $n \sim 290$.

⁴⁸⁰ **B.2 Transparency**

The fraction of ionization electrons transferred through the GEM foil is known as its *transparency*.

$$\text{Transparency} = \frac{\text{Ionized electron transferred through GEM foil}}{\text{Total number of ionized electrons}} \quad (\text{B.3})$$

⁴⁸¹ This is important while finding out the energy resolution and directly effects the
⁴⁸² gain/efficiency of detection.

⁴⁸³ **B.3 Charge-up effect**

⁴⁸⁴ The effect caused by the the electrons or ions coming from the primary or secondary
⁴⁸⁵ ionization from the amplification region sticks to the insulator surface inside the GEM
⁴⁸⁶ holes, which lead to the modification of electric field in the holes and is known as the
⁴⁸⁷ “ *charge-up effect*”.

⁴⁸⁸ It has direct effect on the electron transparency and the effective gain of the GEM
⁴⁸⁹ detector.

⁴⁹⁰ Also, the charge-up effect depends on the geometry of the holes. For the conical
⁴⁹¹ hole gain increases about 60% than the cylindrical hole. There is no effect of the
⁴⁹² charge-up for the cylindrical hole.

⁴⁹³ **B.4 Townsend coefficient**

The probability of ionization per unit path length is known as *First Townsend Coefficient*. It is also defined as the inverse of mean free path.

$$\alpha = \frac{1}{\lambda_{ion}} \quad (\text{B.4})$$

Also, number of secondary ionization created is given as:

$$dn = n \cdot \alpha \cdot dx \quad (\text{B.5})$$

$$n = n_0 e^{\alpha \cdot x} \quad (\text{B.6})$$

Thus, gain will be

$$Gain = \frac{n}{n_0} = e^{\alpha \cdot x} \quad (\text{B.7})$$

⁴⁹⁴ **B.5 Raether Limit**

After a certain critical limit, $Q_{critical}$, of the electron amplification the discharge is very likely to occur. This critical limit is known as the “**Raether limit**”. It is also given as:

$$Q_{critical} = A_{max} \cdot n_0 \quad (\text{B.8})$$

⁴⁹⁵ where, A_{max} is the maximum effective gain achieved by a gaseous detector and n_0 is

⁴⁹⁶ the number of primary ionization electrons.

⁴⁹⁷ **B.6 Collection efficiency**

Collection efficiency is the ratio of the total electrons released from the bottom of GEM foil (last GEM foil in case of multiple foil used) to the number of electrons reached the readout board.

$$\text{Collection efficiency} = \frac{\text{Number of electrons reached readout board}}{\text{Total number of released electron from bottom of GEM foil}} \quad (\text{B.9})$$

⁴⁹⁸ Also, it depends on the ratio of the conversion electric field to the collection elec-
⁴⁹⁹ tric field. Higher the conversion field lesser the collection efficiency. In general the
⁵⁰⁰ conversion field should never be greater than the collection field.

501 **Appendix C**

502 **GE1/1 measured parameters**

503 In lab at CERN several parameters of the tested GE1/1 detectors are measured. They
 504 are - electric field, voltage across each GEM foil, gain and rate for both GE1/1, i.e.,
 505 GE11_IV and GE11_IV_GIF.

The high voltage configuration used during the beam test is shown in Fig. C.1.

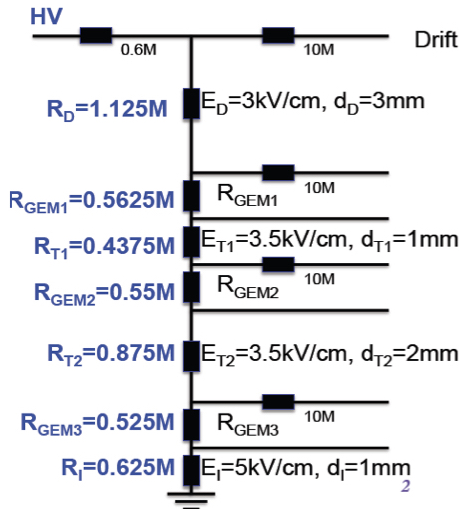


Figure C.1: High voltage divider configuration as used in the 2014 beam test campaign.

506

507 Also, the voltage across the GEM foils and the electric field with respect to the

current in the voltage divider is shown in Fig. C.2.

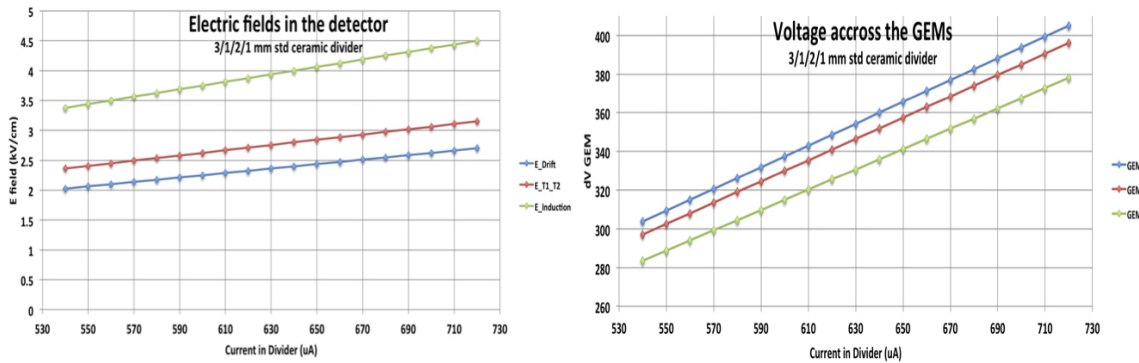


Figure C.2: Electric field (left) and voltage across each GEM foil (right) for the tested GE1/1 detector.

508

509

The gain of the detector was measured in the lab using an X-ray source for both $Ar : CO_2$ and $Ar : CO_2 : CF_4$ gas mixture and is shown in Fig. C.4 and C.3.

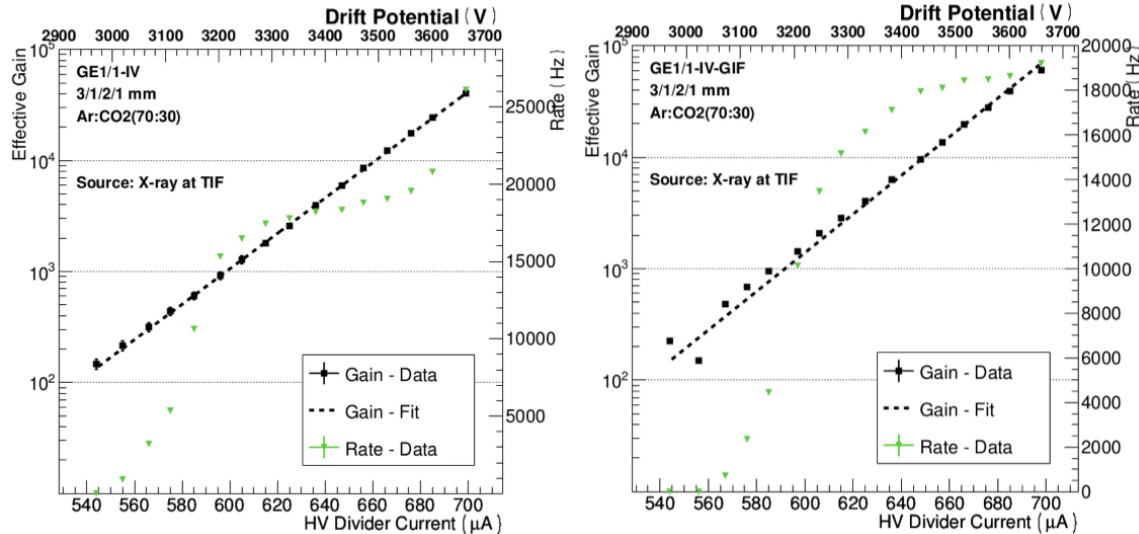


Figure C.3: Gain and rate variation for $Ar : CO_2$ (70:30) with respect to the current supplied to the high voltage divider for GE1/1-IV (left) and GE1/1-IV-GIF (right).

510

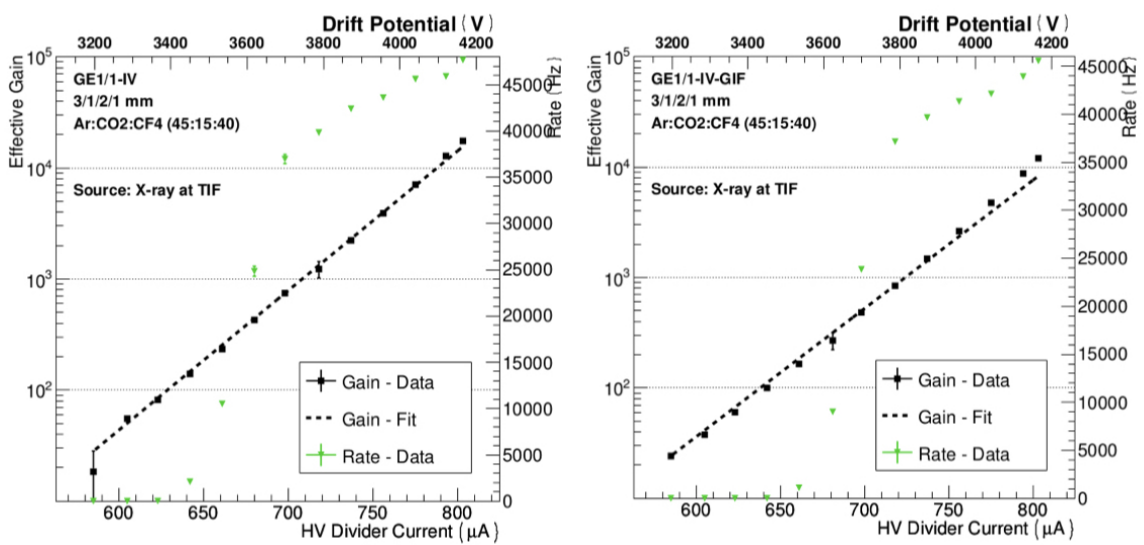


Figure C.4: Gain and rate variation for $Ar : CO_2 : CF_4$ (45:15:40) with respect to the current supplied to the high voltage divider for GE1/1-IV (left) and GE1/1-IV-GIF (right).

511 **Appendix D**

512 **Efficiency and Time Resolution Fit**

513 **Parameters**

514 **D.1 Efficiency Vs E_{gain}**

Here, the efficiency is fitted with function:

$$Efficiency = \frac{Eff_{max}}{1 + e^{s(HV - HV_{50\%})}} \quad (\text{D.1})$$

515 Where, Eff_{max} is the maximum obtained efficiency, $HV_{50\%}$ is the applied HV (or
516 current or E_{gain}) when corresponding efficiency becomes 50% and s is just a scale
517 factor.

518 **D.1.1 Fit Parameters**

519 Let us define four different functions based on equation [D.11](#), F1 for $(i\eta, i\phi)$ sector
520 (5,2) with gas $Ar/CO_2/CF_4$, F2 for $(i\eta, i\phi)$ sector (1,2) with gas $Ar/CO_2/CF_4$, F3
521 for $(i\eta, i\phi)$ sector (8,2) with gas $Ar/CO_2/CF_4$ and F4 for $(i\eta, i\phi)$ sector (5,2) with

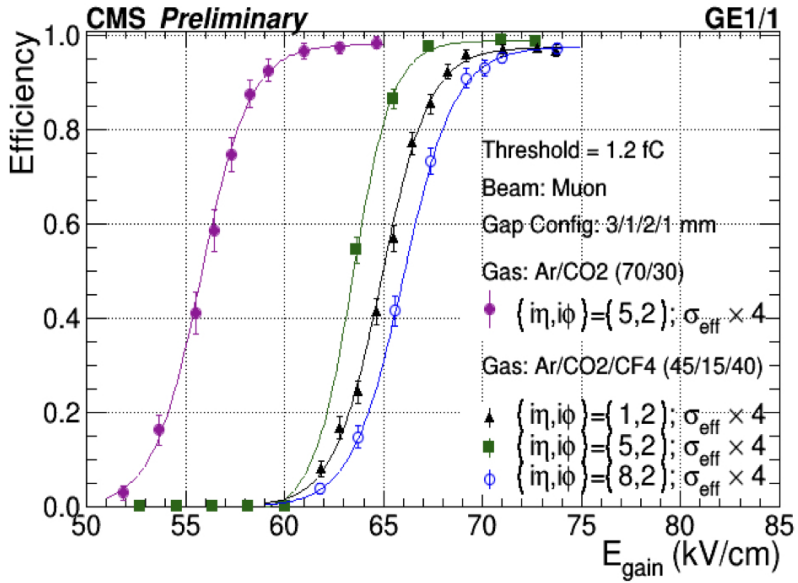


Figure D.1: Efficiency w.r.t. E_{gain} for two different gases and three different $(i\eta, i\phi)$ sectors.

₅₂₂ gas Ar/CO_2 .

After fit F1 is given as

$$F1 = [0] + \frac{0.989}{[1] + \exp(-[2] \times (x - 63.43))} \quad (D.2)$$

where,

$$[0] = -1.44526e - 02 \pm 4.28771e - 02,$$

$$[1] = 9.84833e - 01 \pm 4.19715e - 02, \text{ and}$$

$$[2] = 9.97591e - 01 \pm 8.53940e - 02$$

After fit F2 is given as

$$F2 = \frac{0.968}{[0] + \exp(-[1] \times (x - 64.9))} \quad (\text{D.3})$$

where,

$$\begin{aligned}[0] &= 9.92180e - 01 \pm 5.56034e - 03, \\ [1] &= 8.25180e - 01 \pm 3.62098e - 02\end{aligned}$$

After fit F3 is given as

$$F3 = \frac{0.973}{[0] + \exp(-[1] \times (x - 66))} \quad (\text{D.4})$$

where,

$$\begin{aligned}[0] &= 9.96407e - 01 \pm 9.00503e - 03, \\ [1] &= 7.67029e - 01 \pm 4.59276e - 02\end{aligned}$$

After fit F4 is given as

$$F4 = \frac{0.985}{[0] + \exp(-[1] \times (x - 55.8))} \quad (\text{D.5})$$

where,

$$\begin{aligned}[0] &= 1.00305e + 00 \pm 7.91473e - 03, \\ [1] &= 8.15287e - 01 \pm 5.46309e - 02\end{aligned}$$

⁵²³ **D.2 Efficiency Vs current**

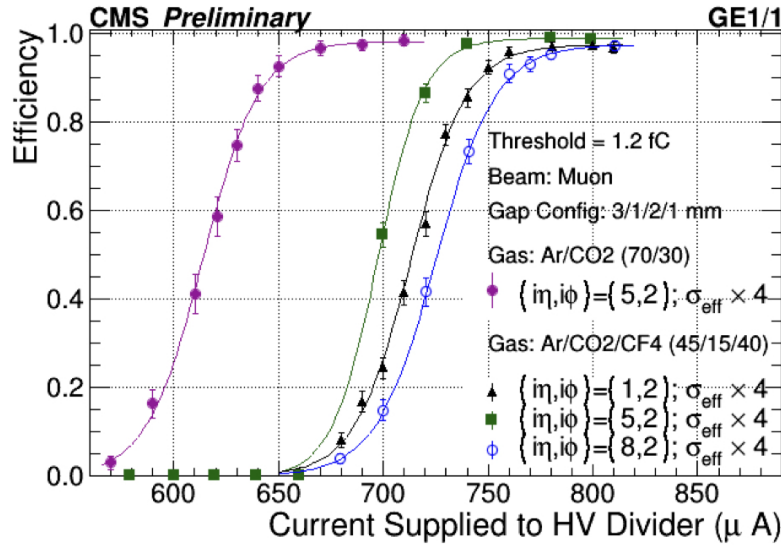


Figure D.2: Efficiency w.r.t. current supplied to high voltage divider for two different gases and three different ($i\eta, i\phi$) sectors.

Here, the efficiency is fitted with function:

$$Efficiency = \frac{Eff_{max}}{1 + e^{s(HV - HV_{50\%})}} \quad (D.6)$$

⁵²⁴ Where, Eff_{max} is the maximum obtained efficiency, $HV_{50\%}$ is the applied HV (or
⁵²⁵ current or E_{gain}) when corresponding efficiency becomes 50% and s is just a scale
⁵²⁶ factor.

⁵²⁷ **D.2.1 Fit Parameters**

⁵²⁸ Let us define four different function, based on equation D.11, F1 for ($i\eta, i\phi$) sector
⁵²⁹ (5,2) with gas $Ar/CO_2/CF_4$, F2 for ($i\eta, i\phi$) sector (1,2) with gas $Ar/CO_2/CF_4$, F3

530 for $(i\eta, i\phi)$ sector (8,2) with gas $Ar/CO_2/CF_4$ and F4 for $(i\eta, i\phi)$ sector (5,2) with
 531 gas Ar/CO_2 .

After fit F1 is given as

$$F1 = [0] + \frac{0.989}{[1] + \exp(-[2] \times (x - 697.3))} \quad (\text{D.7})$$

where,

$$[0] = -1.44526e - 02 \pm 4.28771e - 02,$$

$$[1] = 9.84833e - 01 \pm 4.19715e - 02, \text{ and}$$

$$[2] = 9.97591e - 01 \pm 8.53940e - 02$$

After fit F2 is given as

$$F2 = \frac{0.968}{[0] + \exp(-[1] \times (x - 64.9))} \quad (\text{D.8})$$

where,

$$[0] = 9.92180e - 01 \pm 5.56034e - 03,$$

$$[1] = 8.25180e - 01 \pm 3.62098e - 02$$

After fit F3 is given as

$$F3 = \frac{0.973}{[0] + \exp(-[1] \times (x - 66))} \quad (\text{D.9})$$

where,

$$[0] = 9.96407e - 01 \pm 9.00503e - 03,$$

$$[1] = 7.67029e - 01 \pm 4.59276e - 02$$

After fit F4 is given as

$$F4 = \frac{0.985}{[0] + \exp(-[1] \times (x - 55.8))} \quad (\text{D.10})$$

where,

$$[0] = 1.00305e + 00 \pm 7.91473e - 03,$$

$$[1] = 8.15287e - 01 \pm 5.46309e - 02$$

⁵³² D.3 Efficiency Vs Drift Voltage

Here, the efficiency is fitted with function:

$$\text{Efficiency} = \frac{\text{Eff}_{max}}{1 + e^{s(HV - HV_{50\%})}} \quad (\text{D.11})$$

⁵³³ Where, Eff_{max} is the maximum obtained efficiency, $HV_{50\%}$ is the applied HV (or
⁵³⁴ current or E_{gain}) when corresponding efficiency becomes 50% and s is just a scale
⁵³⁵ factor.

⁵³⁶ D.3.1 Fit Parameters

⁵³⁷ Let us define four different function, based on equation [D.11](#), F1 for $(i\eta, i\phi)$ sector
⁵³⁸ (5,2) with gas $Ar/CO_2/CF_4$, F2 for $(i\eta, i\phi)$ sector (1,2) with gas $Ar/CO_2/CF_4$, F3

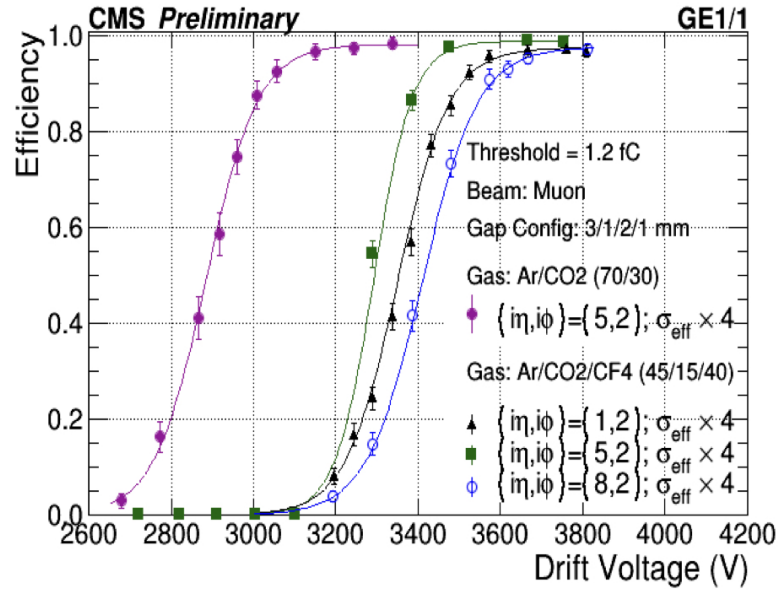


Figure D.3: Efficiency w.r.t. drift voltage for two different gases and three different ($i\eta, i\phi$) sectors.

for ($i\eta, i\phi$) sector (8,2) with gas $Ar/CO_2/CF_4$ and F4 for ($i\eta, i\phi$) sector (5,2) with gas Ar/CO_2 .

After fit F1 is given as

$$F1 = [0] + \frac{0.989}{[1] + \exp(-[2] \times (x - 697.3))} \quad (D.12)$$

where,

$$[0] = -1.44526e - 02 \pm 4.28771e - 02,$$

$$[1] = 9.84833e - 01 \pm 4.19715e - 02, \text{ and}$$

$$[2] = 9.97591e - 01 \pm 8.53940e - 02$$

After fit F2 is given as

$$F2 = \frac{0.968}{[0] + \exp(-[1] \times (x - 64.9))} \quad (\text{D.13})$$

where,

$$\begin{aligned}[0] &= 9.92180e - 01 \pm 5.56034e - 03, \\ [1] &= 8.25180e - 01 \pm 3.62098e - 02\end{aligned}$$

After fit F3 is given as

$$F3 = \frac{0.973}{[0] + \exp(-[1] \times (x - 66))} \quad (\text{D.14})$$

where,

$$\begin{aligned}[0] &= 9.96407e - 01 \pm 9.00503e - 03, \\ [1] &= 7.67029e - 01 \pm 4.59276e - 02\end{aligned}$$

After fit F4 is given as

$$F4 = \frac{0.985}{[0] + \exp(-[1] \times (x - 55.8))} \quad (\text{D.15})$$

where,

$$\begin{aligned}[0] &= 1.00305e + 00 \pm 7.91473e - 03, \\ [1] &= 8.15287e - 01 \pm 5.46309e - 02\end{aligned}$$

541

Bibliography

- 542 [1] G. Charpak et al. “The use of multiwire proportional counters to select and
543 localize charged particles”. In: *Nuclear Instruments and Methods* 62.3 (1968),
544 pp. 262–268. DOI: [10.1016/0029-554x\(68\)90371-6](https://doi.org/10.1016/0029-554x(68)90371-6).
- 545 [2] F. Sauli. “GEM: A new concept for electron amplification in gas detectors”.
546 In: *Nuclear Instruments and Methods in Physics Research Section A: Accelerators, Spectrometers, Detectors and Associated Equipment* 386.2-3 (Feb. 1997),
547 pp. 531–534. DOI: [10.1016/s0168-9002\(96\)01172-2](https://doi.org/10.1016/s0168-9002(96)01172-2).
- 549 [3] Fabio Sauli and Archana Sharma. “Micropattern Gaseous Detectors”. In: *Annual Review of Nuclear and Particle Science* 49.1 (1999), pp. 341–388. DOI:
550 [10.1146/annurev.nucl.49.1.341](https://doi.org/10.1146/annurev.nucl.49.1.341).
- 552 [4] “A GEM of a detector”. In: *CERN Courier* 38.9 (Dec. 1998), pp. 19–20. URL:
553 <https://cds.cern.ch/record/1732870>.
- 554 [5] Maxim Titov. “Radiation damage and long-term ageing in gas detectors”. In:
555 *Innovative Detectors for Supercolliders*. WORLD SCIENTIFIC, 2004. DOI: [10.1142/9789812702951_0014](https://doi.org/10.1142/9789812702951_0014).
- 557 [6] M. Titov et al. “Summary and outlook of the international workshop on aging
558 phenomena in gaseous detectors (DESY, Hamburg, October 2001)”. In: *IEEE*

- 559 *Transactions on Nuclear Science* 49.4 (2002), pp. 1609–1621. DOI: [10.1109/tns.2002.801666](https://doi.org/10.1109/tns.2002.801666).
- 560
- 561 [7] *Kapton Sheet (Tradename of Du Pont Co., Wilmington, DE, USA)*. URL: <http://www.dupont.com/products-and-services/membranes-films/polyimide-films/brands/kapton-polyimide-film.html>.
- 562
- 563
- 564 [8] J. Benlloch et al. “Development of the gas electron multiplier (GEM)”. In: *IEEE Transactions on Nuclear Science* 45.3 (1998), pp. 234–243. DOI: [10.1109/23.682386](https://doi.org/10.1109/23.682386).
- 565
- 566
- 567 [9] S. Bachmann et al. “Discharge studies and prevention in the gas electron multiplier (GEM)”. In: *Nuclear Instruments and Methods in Physics Research Section A: Accelerators, Spectrometers, Detectors and Associated Equipment* 479.2-3 (2002), pp. 294–308. DOI: [10.1016/s0168-9002\(01\)00931-7](https://doi.org/10.1016/s0168-9002(01)00931-7).
- 568
- 569
- 570
- 571 [10] A Colaleo et al. *CMS Technical Design Report for the Muon Endcap GEM Upgrade*. Tech. rep. CERN-LHCC-2015-012. CMS-TDR-013. June 2015. URL: <https://cds.cern.ch/record/2021453>.
- 572
- 573
- 574 [11] Jeremie Alexandre Merlin. “Study of long-term operation of triple-GEM detectors for the high rate environment in CMS”. In: CMS-CR-2013-279. Oct. 2013.
- 575
- 576 URL: <https://cds.cern.ch/record/1621595>.
- 577
- 578
- 579
- 580 [12] P Aspell et al. *VFAT2: A front-end system on chip providing fast trigger information, digitized data storage and formatting for the charge sensitive readout of multi-channel silicon and gas particle detectors*. eng. 2007. DOI: [10.5170/cern-2007-007.292](https://doi.org/10.5170/cern-2007-007.292).
- 581
- 582
- 583 [13] V Berardi et al. *TOTEM: Technical Design Report*. Tech. rep. CERN-LHCC-2004-002 ; TOTEM-TDR-001. 2004. URL: [http://cds.cern.ch/record/704349](https://cds.cern.ch/record/704349).

- 584 [14] F. Licciulli et al. “Calibration, bias and monitoring system for the VFAT3 ASIC
585 of the CMS GEM detector”. In: *2017 7th IEEE International Workshop on*
586 *Advances in Sensors and Interfaces (IWASI)*. IEEE, 2017. DOI: [10.1109/iwasi.2017.7974222](https://doi.org/10.1109/iwasi.2017.7974222).
- 588 [15] Roberto Cecchi and Maria Grazia Bagliesi. “The Turbo Board and Software”.
589 Siena University. May 2011. URL: <https://indico.cern.ch/event/136793/contributions/1360602/attachments/112026/159286/TURBO-PaulMeeting.pdf>.
- 591 [16] P. Aspell et al. “The VFAT production test platform for the TOTEM experiment”. In: *Electronics for particle physics. Proceedings, Topical Workshop, TWEPP-08, Naxos, Greece, 15-19 September 2008*. 2008, pp. 544–548. URL: <http://doc.cern.ch/yellowrep/2008/2008-008/p544.pdf>.
- 596 [17] TOTEM group. *TurboSoftware*. GitHub. Updated by Ram Krishna Sharma for
597 CMS GEM test beam. URL: <https://github.com/ram1123/TurboSoftware>.
- 598 [18] Rui DE OLIVEIRA and Serge DUARTE PINTO. “A METHOD OF MANU-
599 FACTURING A GAS ELECTRON MULTIPLIER”. English. Pat. WO/2009/127220.
600 Oct. 2009. URL: <https://patentscope.wipo.int/search/en/detail.jsf?docId=W02009127220&recNum=&maxRec=1000&office=&prevFilter=&sortOption=&queryString=&tab=PCTBiblio>.
- 603 [19] KANOMAX dust particle counter Model 3887. URL: https://www.kanomax-usa.com/wp-content/uploads/2015/10/3887_manual.pdf.
- 605 [20] S. Bachmann et al. “Charge amplification and transfer processes in the gas elec-
606 tron multiplier”. In: *Nuclear Instruments and Methods in Physics Research Sec-*
607 *tion A: Accelerators, Spectrometers, Detectors and Associated Equipment* 438.2-
608 3 (1999), pp. 376–408. DOI: [10.1016/s0168-9002\(99\)00820-7](https://doi.org/10.1016/s0168-9002(99)00820-7).

- 609 [21] M. Posik and B. Surrow. “Optical and electrical performance of commercially
610 manufactured large GEM foils”. In: *Nuclear Instruments and Methods in Physics*
611 *Research Section A: Accelerators, Spectrometers, Detectors and Associated Equipment* 802 (2015), pp. 10–15. DOI: [10.1016/j.nima.2015.08.048](https://doi.org/10.1016/j.nima.2015.08.048).
- 612
613 [22] Ulrich Becker, Brian Tamm, and Scott Hertel. “Test and evaluation of new
614 GEMs with an automatic scanner”. In: *Nuclear Instruments and Methods in*
615 *Physics Research Section A: Accelerators, Spectrometers, Detectors and Associated*
616 *Equipment* 556.2 (2006), pp. 527–534. DOI: [10.1016/j.nima.2005.11.056](https://doi.org/10.1016/j.nima.2005.11.056).
- 617 [23] D. Abbaneo et al. “Quality control and beam test of GEM detectors for fu-
618 ture upgrades of the CMS muon high rate region at the LHC”. In: *Journal*
619 *of Instrumentation* 10.03 (2015), pp. C03039–C03039. DOI: [10.1088/1748-0221/10/03/c03039](https://doi.org/10.1088/1748-0221/10/03/c03039).
- 620
621 [24] *MIT Megger 420*. URL: <https://www.instrumart.com/products/35023/megger-mit420-insulation-tester>.
- 622
623 [25] *Keithley 6517B picoammeter*. URL: <https://www.tek.com/keithley-low-level-sensitive-and-specialty-instruments/keithley-high-resistance-low-current-electrom>.
- 624
625
626 [26] D Abbaneo et al. “Characterization of GEM detectors for application in the
627 CMS muon detection system”. In: *IEEE Nuclear Science Symposium & Medical*
628 *Imaging Conference*. IEEE, 2010. DOI: [10.1109/nssmic.2010.5874006](https://doi.org/10.1109/nssmic.2010.5874006).
- 629
630 [27] D. Abbaneo et al. “Test beam results of the GE1/1 prototype for a future up-
631 grade of the CMS high- η muon system”. In: *2011 IEEE Nuclear Science Sym-*
posium Conference Record. IEEE, 2011. DOI: [10.1109/nssmic.2011.6154688](https://doi.org/10.1109/nssmic.2011.6154688).

- 632 [28] D. Abbaneo et al. “Beam test results for new full-scale GEM prototypes for
633 a future upgrade of the CMS high- η Muon System”. In: *2012 IEEE Nuclear*
634 *Science Symposium and Medical Imaging Conference Record (NSS/MIC)*. IEEE,
635 Oct. 2012. doi: [10.1109/nssmic.2012.6551293](https://doi.org/10.1109/nssmic.2012.6551293).
- 636 [29] D. Abbaneo et al. “The status of the GEM project for CMS high- η muon sys-
637 tem”. In: *Nuclear Instruments and Methods in Physics Research Section A:*
638 *Accelerators, Spectrometers, Detectors and Associated Equipment* 732 (2013),
639 pp. 203–207. doi: [10.1016/j.nima.2013.08.015](https://doi.org/10.1016/j.nima.2013.08.015).